Wave and vibration attenuation in graded elastic metamaterial beams with local resonators

C.B.F. Gomes[a], M.C.P. dos Santos[a], B.C.C. Araújo[a], F.N. Pereira[b], E.D. Nobrega[c], J.M.C. Dos Santos[d], E.J.P. Miranda Jr.[a,e,f,*], A. Sinatora[f]

[a] *Federal Institute of Maranhão, IFMA-PPGCTM, Avenida Getúlio Vargas, 4, CEP 65030-005, São Luís, MA, Brazil.*
[b] *State University of Maranhão, UEMA-CCT-DEMEC, Rua Paulo VI, s/n, CEP 65055-970, São Luís, MA, Brazil*
[c] *Federal University of Maranhão, UFMA-CCET-CCEM, Avenida dos Portugueses, 1966, CEP 65080-805, São Luís, MA, Brazil.*
[d] *University of Campinas, UNICAMP-FEM-DMC, Rua Mendeleyev, 200, CEP 13083-970, Campinas, SP, Brazil.*
[e] *Federal Institute of Maranhão, IFMA-EIB-DE, Rua Afonso Pena, 174, CEP 65010-030, São Luís, MA, Brazil.*
[f] *Vale Institute of Technology, ITV, Rua Professor Paulo Magalhães, CEP 35400-000, Ouro Preto, MG, Brazil.*

Abstract

This study investigated the bending band gaps in an Euler-Bernoulli metamaterial beam with attached mass-spring resonators. The position and mass of the resonators were considered following three different configurations, given by the arithmetic, geometric, and quadratic progressions. With the extended plane wave expansion (EPWE), wave finite element (WFE), and wave spectral element (WSE) methods, complex dispersion diagrams were obtained, where the band gaps due to Bragg scattering and local resonance were analyzed. From the study of vibration via forced response, the results are confirmed also for finite structures. A coupling between locally resonant and first Bragg-type band gaps ($\sim$ 461 Hz) was observed considering a set of $N = 10$ resonators, increasing the wave attenuation region. The wave propagation and forced response simulations showed that the grading of the resonators' positions can modulate the coupling between local resonance and Bragg band gaps, demonstrating the potential to enhance attenuation by leveraging the natural vibration frequency of graded

*Corresponding author. Tel.: +55 9832226350
Email address: edson.jansen@ifma.edu.br (E.J.P. Miranda Jr.)

resonators. The influence of the resonator mass was studied through parametric diagrams, where the change of the smallest part of the imaginary component of Bloch wave vector with the increase of the ratio between the mass of the resonators and the unit cell of the bare beam was observed. The dispersion diagrams and forced responses indicated that the best dynamic performance in terms of wave and vibration attenuation was obtained for simultaneous geometric progression in the resonator's positions and arithmetic progression in the resonator's mass, respectively.

Keywords: Graded metamaterial beams, flexural wave propagation, vibration reduction, resonator position, local resonance, band gap coupling.

---

1. Introduction

Mechanical metamaterials (MMs), also known as elastic metamaterials or locally resonant phononic crystals (PCs), are artificial materials designed to achieve unusual mechanical performance such as negative thermal expansion [1, 2], and negative Poisson's ratio [3–5]. Furthermore, MMs exhibit extraordinary dynamic behavior, as detailed in [6–10].

An important property of MMs are the so called stop bands, or band gaps, in the dispersion diagrams, which are frequency ranges where there are only evanescent wave modes [11–14]. The band gaps in periodic MMs are opened due to the local resonance phenomena and the Bragg scattering mechanism. Locally resonant band gaps arise on the vicinity of resonator's natural frequency and they do not depend on periodicity, while Bragg-type band gaps typically occur at wave lengths of the order of unit cell size [15–23].

With the advances of additive manufacturing and 3D printing, the study and design of MMs have been a current research topic and bring promising prospects for engineering problems [24–32]. An important structure used in problems of vibration attenuation is the MM Euler-Bernoulli beam [33, 34], which can be built in a simple version from a set of resonators attached to the beam. In Ref. [17], the authors demonstrated the existence of local resonance

in a beam containing multiple periodic arrays of attached resonators. In this case, the plane wave expansion (PWE) and the extended plane wave expansion (EPWE) methods were employed to obtain the band structure, which revealed the band gaps near the natural frequency of the resonators and the respective band gaps in the regions of the Bragg condition. In the context of beams with resonators, several other configurations were investigated [35–39], such as the inclusion of vibration absorbers [40], a set of resonators with several degrees of freedom (DOFs) coupled to the beam [41], a sandwich of beams interconnected by resonators with one [42], and two [43] DOFs.

Graded materials are those in which their structural elements themselves have a specific arrangement. They can be found in nature or artificially designed. Therefore, elucidating the effects of gradation features enables the design of materials with physical properties tailored for specific applications [44]. Recently, the concepts of graded materials and MMs have been combined, and researchers have found that considering graded features in the design parameters can modify the dynamic performance of metamaterials [45–56]. Extensive studies investigate the band structure of MMs in the context of beams with attached spring-mass resonators associated with graded structures [57–60]. In Ref. [59] the effect of graded variation of mass and distance between successive resonators in a MM beam is studied. It was observed that the flexural band structure is highly sensitive to the natural frequency and the distance between the resonators, and that the low frequency band gaps are shifted or widened in this type of arrangement. Furthermore, in Ref. [60], the authors investigated a graded metamaterial beam for broadband vibration suppression, conducting a parametric study to reveal the effects of the frequency spacing and damping ratio on the dynamic behavior of the structure. Within an engineering framework, metamaterial beams with periodic graded resonators have been proposed for energy harvesting [61–63], energy trapping, confinement, and amplification [64, 65], mode conversion [66], micro-electromechanical systems (MEMS) [67, 68], low frequency broadband sound absorption, and waveguides [69, 70].

In this work, the complex dispersion diagrams and forced responses were computed by considering flexural wave propagation in a 1-D graded metamaterial Euler-Bernoulli beam. The results analyzed how gradation influences the wave and vibration attenuation in a MM beam with attached resonators. Unlike previous studies, our approach uses the PWE, EPWE, wave finite element (WFE), and wave spectral element (WSE) methods to comprehensively investigate the effects of resonator position and mass configurations on the beam's band structure. This multi-method approach for calculating the dispersion diagrams and forced responses allows for a more thorough understanding of how different resonator arrangements impact the band gap and attenuation zones characteristics, offering insights for optimized elastic metamaterials. Furthermore, the effect of the gradation on the coupling between the Bragg and local resonance band gaps is explored, with emphasis placed on its role in expanding attenuation regions, which contributes to the improved performance of metamaterials in practical applications.

This paper is organized as follows. In section 2, the Euler-Bernoulli metamaterial beam model is introduced, as well as the Floquet-Bloch periodic condition for the 1-D periodicity. The effect of position and mass gradations of the resonators on both the band structure and forced responses are reported in Section 3. The paper is concluded in Section 4. The derivations regarding the PWE, EPWE, WFE, and WSE methods applied for the study of the graded locally resonant (LR) metamaterial beam are shown in Appendix A, Appendix B, Appendix C, and Appendix D, respectively.

2. Graded elastic metamaterial beam modelling

In this section, the metamaterial model, Floquet-Bloch periodic conditions, and concept of the reciprocal lattices are defined. A homogeneous beam with multiple mass-spring resonators periodically attached is considered in this study. The PWE method was used to compute the real part of the wave number as a function of the frequency, i.e., the real part of the dispersion relation, where only

propagating wave modes are obtained. EPWE method was used to obtain the imaginary and complex parts of the dispersion diagram (i.e., both propagating and evanescent wave modes are obtained), while WFE, and WSE methods were used to compute both the complex dispersion relation and frequency response function (FRF). Furthermore, alternative aproaches are available to analyze the dispersive behavior of such structures, such as the Cauchy formalism [71, 72] and Stroh formalism [73] which are free from simplified beam hypothesis. In this graded LR metamaterial beam, there are N resonators in each unit cell. The jth resonator of an arbitrary unit cell presents mass m_j, position x_j, spring constant k_j, and natural frequency f_j. The schematic of this model is available in Fig. 1. A particular configuration of the graded LR metamaterial beam is discussed in the results, where the resonators present the same mass, i.e., the graded feature is considered only in the position (or spatial distribution) of the resonators.

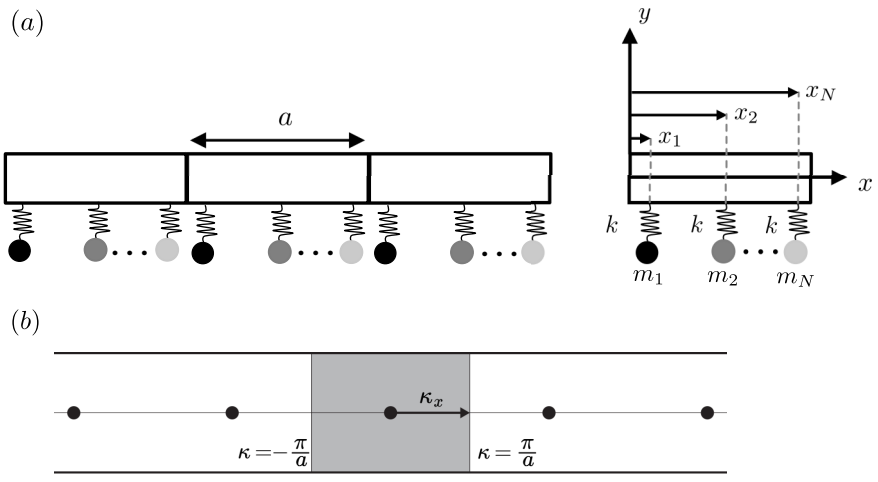

Figure 1: Schematic of the graded beam with attached spring-mass resonators (a) and (b) reciprocal lattice in one dimensional periodicity. The First Brillouin zone boundaries are highlighted at $\kappa = \pm\pi/a$, and $\kappa_x = \kappa$ is the Bloch wave vector. The unit cell of the crystal structure contains a lattice constant a, N resonators with different positions ($x_1,\ x_2,\ \cdots,\ x_N$), masses ($m_1,\ m_2,\ \cdots,\ m_N$), and natural frequencies ($f_1,\ f_2,\ \cdots,\ f_N$).

According to the Euler-Bernoulli beam theory, the equation of motion of

bending waves in homogeneous beams is given by

$$EI\frac{\partial^4}{\partial x^4}\hat{u}(x,t)+\rho S\frac{\partial^2}{\partial t^2}\hat{u}(x,t)=\hat{p}(x,t), \tag{1}$$

where $\hat{u}(x,t)$ is the transversal displacement in time domain, E is the Young's modulus, I is the second moment of area, ρ is the density, S is the cross-sectional area of the beam, and $\hat{p}(x,t)$ is an external force related to the mass-spring resonator assembly.

Considering the graded LR metamaterial beam in Fig. 1 as infinite for the dispersion diagram computation, periodic solutions of the displacement in Eq. (1) in the frequency domain can be derived from Floquet-Bloch's theorem:

$$u(x,\omega)=e^{-i\kappa(\omega)x}u_\kappa(x), \tag{2}$$

where $u_\kappa(x)$ is the Bloch wave amplitude, $\kappa_x=\kappa$ is the Bloch wave vector, also known as wave number, restricted to the first Brillouin zone (FBZ), $[-\pi/a,\pi/a]$, depicted in Fig. 1b, or first irreducible Brillouin zone (FIBZ), $[0,\pi/a]$, and $i=\sqrt{-1}$ is the complex unity. In addition, periodic boundary conditions implies that $u(x_j+a,\omega)=u(x_j)e^{-i\kappa(\omega)a}$ and $w_j(x_j+a,\omega)=w_j(x_j)e^{-i\kappa(\omega)a}$, where the exponential $e^{-i\kappa a}$ is called Floquet-Bloch's periodic boundary condition.

3. Simulated examples

In this section, the results of unit cell wave attenuation in the graded LR metamaterial beam considering gradation in position, subsection 3.1, and simultaneously in position and mass of the resonator array, subsection 3.2, following arithmetic progression (AP), geometric progression (GP), and quadratic progression (QP) are presented. The dynamic analysis is performed using PWE, EPWE, WFE, and WSE methods. For all examples, the geometry and material properties of the graded LR metamaterial beam are the same as shown in Table 1. It should be mentioned that considering a structural damping for the beam (η_b) and resonator (η_r) materials it is similar to model these materials with a Kelvin-Voigt viscoelasticity [45]. However, there are other more complex

viscoelastic models [74–77] that should be investigated in the future, since it also influences the wave and vibration attenuation of the structure. Regarding the numerical methods for the dynamic analysis of the LR graded metamaterial beam, the 1-D Euler-Bernoulli beam element was considered, therefore with two degrees of freedom in each element node. The spectral element discretization was considered in such a way that each resonator in a unit cell coincides with the spectral element node, i.e., a discontinuity in the model. The wave finite element discretization used a partitioning of the unit cell in 20 substructures (slices). The dynamic stiffness matrix for each substructure was, therefore, of order 36.

Table 1: Locally resonant beam geometry and material properties [41].

Geometry/Property	Value
Unit-cell length (a)	0.1 m
Cross-sectional area (S)	4×10^{-5} m^2
Young's modulus (E)	7×10^{10} Pa
Structural damping (η_b, η_r)	0.01, 0.05
Mass density (ρ)	2700 kg/m^3
Second moment of area (I)	1.33×10^{-11} m^4

Following subsequent results, band gaps due to local resonances and those arising from Bragg scattering are presented. It is known that the local resonance mechanism produces band gaps in frequency ranges close to the natural frequencies of the resonant elements. In contrast, Bragg band gaps are expected at $a = m(\lambda/2)$ with $m = 1, 2, 3, ...$, where λ is the wavelength of the waves in the host material. For the case of a LR metamaterial beam with a single set of resonators, the first Bragg band gap frequency is analytically predicted by:

$$f_\mathrm{Bragg} = \frac{1}{2\pi}\left(\frac{\pi}{a}\right)^2\sqrt{\frac{EI}{\rho S}} \approx 461.8 \text{ Hz}. \tag{3}$$

In the simulations arising from the PWE and EPWE methods, only 3 plane waves ($M = 1$) are considered, due to the high convergence performance of

the approaches [41, 78]. The structure proposed by the model presented in Fig. 1 assumes a homogeneous beam, reducing the need for a large number of plane waves to achieve convergence [17, 41]. Generally, the application of both methods to inhomogeneous structures requires a larger number of plane waves to converge the results due to the discrepancy in material properties [79].

The total mass of the resonators can be written in terms of the mass of the unit cell of the beam as

$$M_r = m_1 + m_2 + \ldots + m_N = \sigma_r M_c, \tag{4}$$

where $\sigma_r = \sum_{j=1}^{N} \sigma_j$ represents the fraction of mass that the resonators occupy over the total mass of the resonant structure in a unit cell $M_c = \rho a S$. In all simulations, it was considered a value of $\sigma_r = 0.5$.

3.1. Gradation in the resonator position

In the following analyses, the real and complex dispersion diagrams obtained by the PWE, EPWE, WFE, and WSE methods are presented. The real part of the dispersion curves is obtained using the PWE method, using the $\omega(\kappa)$ approach. Furthermore, the $\kappa(\omega)$ approach is used to calculate the complex dispersion diagram, in which all waves are evanescent, since structural damping is considered, using EPWE, WFE, and WSE methods. The results are obtained considering $N = 10$ resonators per unit cell, both with the same mass m, spring constant k, and natural frequency f.

3.1.1. Arithmetic progression

The grading of resonator positions in terms of an AP is carried out according to the following expression:

$$x_j = x_1 + d(j-1), \tag{5}$$

where, $x_1 = 0$ is the position of the first resonator, placed at the left end of the model, x_j ($j = 1, 2, \ldots, N$) is the position of the jth resonator, and $d = a/N$ is the ratio between the length of the unit cell and the number of resonators.

As an example, it is shown in Fig. 2 the real dispersion diagram, considering only the purely propagating waves, obtained by the PWE method. The dispersion relation of a bare beam (in red), i.e., without attached resonators is also depicted, for comparison purposes. As expected, there is a local resonance band gap in the vicinity of the resonator's natural frequency, i.e., tuned at 200 Hz, while for the bare beam, no band gaps are observed. The LR metamaterial beam with $N = 10$ resonators graded according to arithmetic progression over the unit cell of length a is equivalent to a system with a single resonator attached at position $x_1 = 0$ in a unit cell of length $a/10$. Therefore, in this case the first Bragg band gap is found at a higher frequency, which is not investigated here.

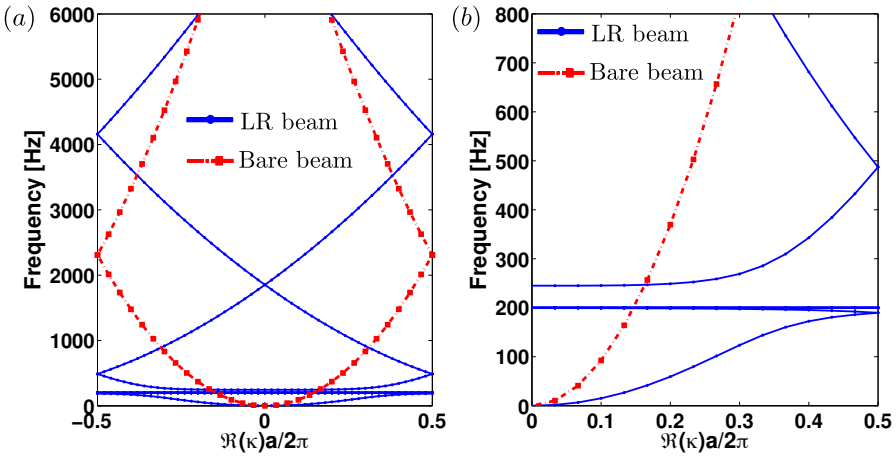

Figure 2: Real (a) part and zoom (b) of the locally resonant band gap of the dispersion diagram for an AP in resonator's position, Eq. (5), and bare beam, calculated by PWE approach considering $N = 10$, $m = \frac{\sigma_r}{N} M_c = 0.54 \times 10^{-3}$ kg, and $f = 200$ Hz.

A typical complex diagram, obtained through the EPWE method (e.g., similar as described in [41]), is depicted in Fig. 3. In this case, evanescent waves are considered, where complex Bloch wave vectors are found. In Fig. 3(a), the real part of the dimensionless Bloch wave vector, $\kappa a/2\pi$, is depicted. It is worth noting that the bands obtained via EPWE are not restricted to their respective original Brillouin zones, and they may cross other regions as the frequency increases

[41]. Furthermore, the results obtained for the interval $\kappa a/2\pi = [-1/2, 1/2]$, are repeated throughout the axis, with intervals of $\kappa a/2\pi = n$ for $n \in \mathbb{Z}$. The imaginary part of the dispersion diagram is presented in Fig. 3(b). From this analysis, the attenuation of waves in the unit cell is studied, where the smallest value (or the most accurate, i.e., components of lower amplitude) of the normalized imaginary wave number, $\kappa a/2\pi$, whose real part is contained within the FBZ, indicates the intensity of the unit cell wave attenuation for each frequency range [17, 41, 45].

The configuration of the complex bands is established through the application of the model assurance criterion (MAC) [80], which assesses the correlation between Bloch wave modes acquired through the EPWE method.

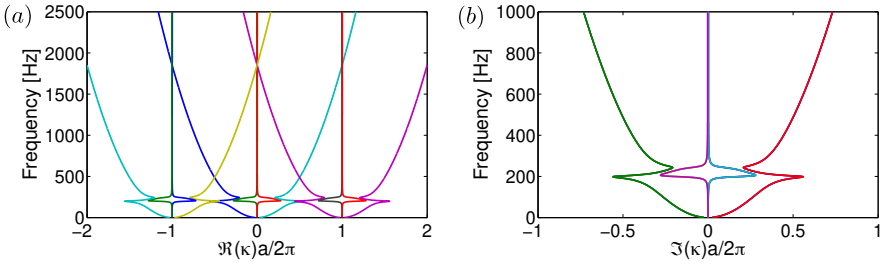

Figure 3: Real (a) and imaginary (b) parts of the dispersion diagram for an AP in resonator's position, Eq. (5), calculated by EPWE considering the same parameters as in Fig. 2.

Figure 4 presents the diagrams of three distinct resonator configurations at $f = 200$ Hz, 460 Hz, and 720 Hz, maintaining the arrangement of positions in terms of the AP. In Fig. 4(a, c, e) (i.e., the left panels), the comparison between the real part of the complex dispersion diagram (obtained by EPWE, lines) and the bands derived from purely propagating waves (obtained by PWE, black circles) is depicted. Due to structural damping, in the entire complex diagram all waves are evanescent, and therefore the comparison with propagating waves highlights the band gap regions. Note that the wave modes obtained by the PWE are not capable of capturing the dispersion effect within the band gaps, as the eigenvalues of ω are purely real. In the right panels (see Figs. 4(b, d, f)), the lowest values of $\Im(\kappa)a/2\pi$ are displayed, emphasizing the attenuation over

the unit cell of each configuration. For the purpose of validation, the EPWE (lines), WFE (dashed lines), and WSE (blue triangles) methods were compared, where a good agreement of both was obtained. As expected, resonant band gaps are observed in the regions of the respective natural frequencies of the resonators f. Furthermore, it is notable that the intensity of attenuation increases with the increment of f.

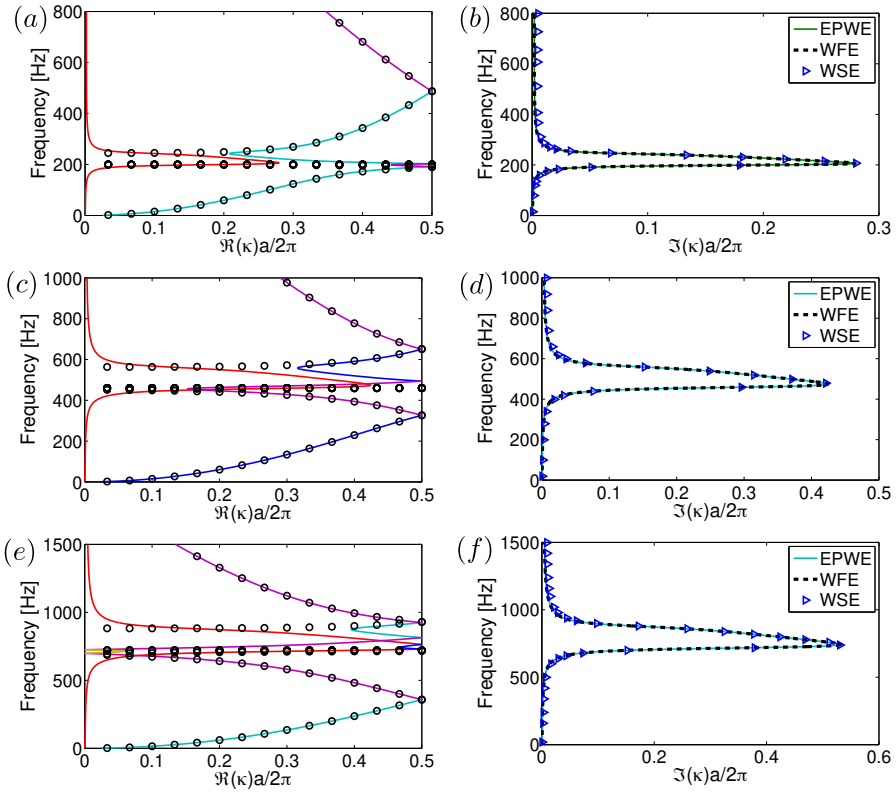

Figure 4: (Left panels) Comparison between the real part of the complex dispersion diagram (EPWE) and the pure real bands (PWE), displayed in solid lines and circles, respectively. (Right panels) The smallest value of the imaginary part of the Bloch wave vector $\Im(\kappa)a/2\pi$ calculated by the EPWE, WFE, and WSE methods. The results are obtained using AP, Eq. (5). The parameters used are: $N = 10$, $m = \frac{\sigma_r}{N} M_c = 0.54 \times 10^{-3}$ kg, (a-b) $f = 200$ Hz, (c-d) $f = 460$ Hz, and (e-f) $f = 720$ Hz.

3.1.2. Geometric progression

For the GP, the resonator position along the LR metamaterial beam can be expressed as:

$$x_j = x_1 r^{j-1}, \tag{6}$$

where $x_1 = a/550$ is the position of the first resonator and $r = 2$ is the common ratio. The nonuniform arrangement of the resonators introduces the gradation in the LR metamaterial beam. In this configuration, different effects are observed in the complex dispersion diagram when compared to the case without gradation represented by the AP.

In imaginary part of the complex dispersion diagrams obtained through EPWE for the graded LR metamaterial beam, a notable feature is the presence of multiple similar curves that overlap around the natural frequency of the resonators. Figure 5 shows an example of the most accurate imaginary mode and its respective real counterpart, showing the greatest evanescent behavior of waves in the vicinity of 200 Hz. In this case, the first Bragg band gap is also found, represented by the small amplitude component around 460 Hz, as shown in Fig. 5(b).

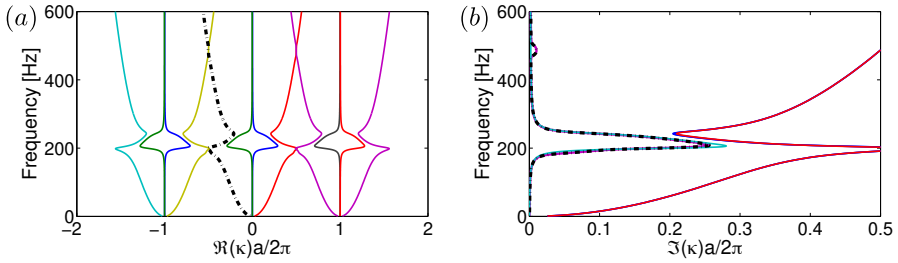

Figure 5: Real (a) and imaginary (b) parts of the complex dispersion diagram for a graded LR metamaterial beam calculated by EPWE. The dot-dashed (black) curves represent the most accurate imaginary component with the smallest amplitude and its real counterpart originating in the FBZ. The position of the resonators is considered as described by a GP. The parameters used are: $N = 10$, $m = \frac{\sigma_r}{N} M_c = 0.54 \times 10^{-3}$ kg, and $f = 200$ Hz.

The complex diagram of the graded LR metamaterial beam, considering the arrangement of the resonators in the unit cell described by GP, Eq. (6), is

shown in Fig. 6. The real part of the dispersion diagram (Fig. 6(a, c, e)) delineates the band gaps, where it is observed that for all frequencies of the studied resonators, the Bragg band gap is observed at approximately 460 Hz. Wave attenuation in the unit cell is observed through the most precise complex modes. In Fig. 6(b), is observed that the attenuation intensity for $f = 200$ Hz is slightly smaller and wider than in the AP case. When the coupling between the Bragg and local resonance band gaps occurs ($f = 460$ Hz), a widening of the attenuation region is observed, as shown in Fig. 6(d). The LR and Bragg type bandgap coupling is a phenomenon reported in literature as a prominent manner of enhancing a metamaterial performance, i.e., broadening vibration attenuation ranges [81–84]. Moreover, the advantage of tuning the resonator resonance close to the Bragg scattering frequency has also been reported for analogous electromechanical systems [85]. However, this effect of widening the wave attenuation region due to the coupling between the two types of band gaps in graded structures is one of the main new findings of this work, showing the possibility of increasing the attenuation controlled by the natural vibration frequency of the resonators.

For f greater than the Bragg frequency, Eq. (3), the EPWE and WFE methods require two wave modes to describe the imaginary part of the Bloch wave vector with the smallest amplitude. Therefore, the most accurate effective wave mode is characterized by the intersection between the modes that produce the smallest amplitude corresponding to the imaginary part of κ, whose respective real parts originate in the FBZ. Note that this characteristic is not reproduced by the WSE method, where the effective wave mode is obtained directly. In the case of attenuation of the unit cell with GP configuration for $f = 720$ Hz, it is observed that there is a widening of the attenuation region (see the blue triangles of WSE), when compared to the case of the beam with the position structure of the resonators given by the AP. For $f = 720$ Hz the Bragg and local resonance bands are practically uncoupled, presenting two attenuation regions separated by a region of propagating waves. These results are shown in Fig. 6(f).

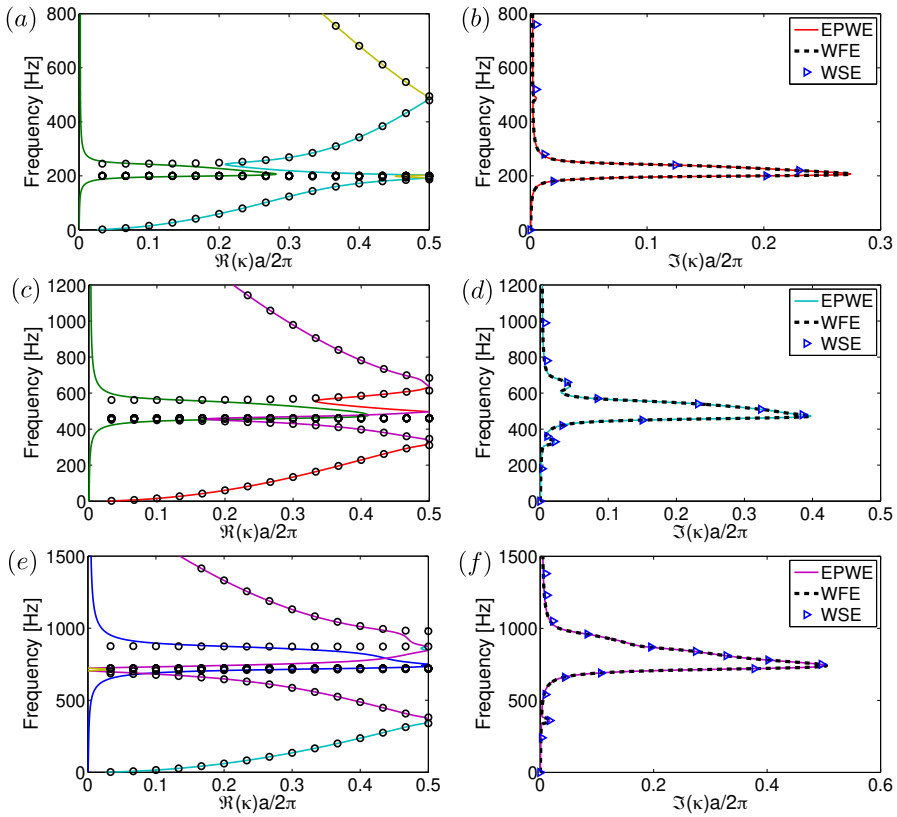

Figure 6: The same as Fig. 4, but considering gradation in the position of the resonators, corresponding to the GP, Eq. (6).

3.1.3. Quadratic progression

A QP is a sequence of numbers where the difference between consecutive terms is not constant (as in AP), but rather increases linearly. This means that the difference between consecutive terms forms an AP. Therefore, the jth resonator position graded to the beam by QP is given by:

$$x_j = x_1 + \beta(j-1)^2, \tag{7}$$

where $x_1 = 0$, $\beta = \dfrac{a}{N^2 - N}$, with $N > 1$.

In Fig. 7, the gradation of the resonator position is considered in the form of QP, Eq. (7). The results of the dispersion diagram derived from purely

propagating waves are different from those presented previously. The evanescent waves present very different results when compared with the AP and GP cases. The highlight of this type of gradation is in the wave attenuation in the unit cell, where differences in the intensity of the band gaps are observed. For example, when comparing the results between QP and GP in the case of Bragg-local resonance coupling, the attenuation observed with QP is more pronounced in the Bragg frequency region. This behavior extends to frequencies higher than f_{Bragg}, where a more significant wave attenuation peak is observed in the unit cell of the QP configuration at $f = 720$ Hz. Additionally, at $f = 720$ Hz, the GP exhibits two distinct attenuation regions (peaks) in the imaginary part of the dispersion diagram, whereas the QP shows only one, but it is more intense.

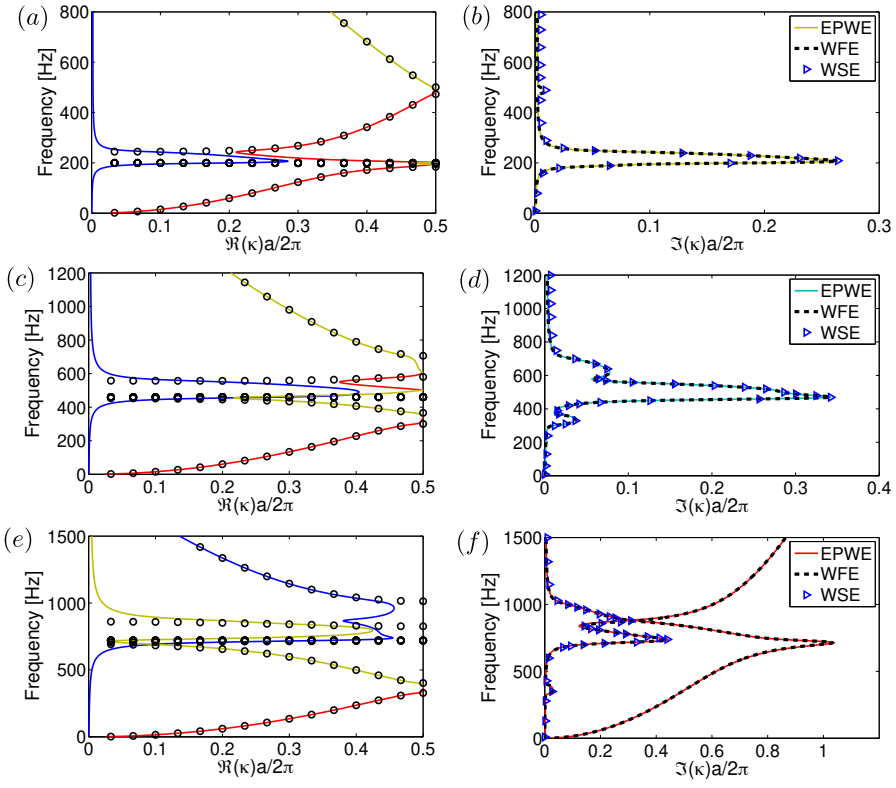

Figure 7: The same as Figs. 4 and 6, but considering gradation in the position of the resonators according to the QP, Eq. (7).

3.1.4. Forced response in the LR metamaterial beam with resonator position gradation

The study of the influence of resonator position configurations on vibration attenuation in finite systems is analyzed in terms of the frequency response function (FRF) of the graded LR metamaterial beam. The considered boundary and loading conditions were, respectively, free-free ends and a unitary force excitation at the left end ($x = 0$) of the beam. This investigation is carried out through receptance, which corresponds to the ratio between the displacement of a node of the beam and the excitation force, where a point at the right end of the graded LR metamaterial beam, on the opposite side of the force application, is considered. All results are obtained with a finite structure of $N_c = 20$ unit cells with material and geometry properties depicted in Table 1.

Figure 8(a) shows the receptance FRF calculated by WSE for the graded LR metamaterial beam with AP, GP, and QP configurations, with resonators tuned at 200 Hz. The boundary conditions considered allow for the evaluation of the influence of resonator positioning on the dynamic behavior of the graded LR metamaterial beam. The results show very similar receptance responses in both configurations. The AP and QP cases present the largest attenuation valleys. Although these results are very similar, the QP configuration shows a slightly greater attenuation region than the AP configuration. In a direct comparison between the configuration of resonator positions, the GP structure presents a slightly larger wave attenuation width than the AP and QP. These results are confirmed by the minimum value of the imaginary part of the reduced Bloch wave vector in Fig. 8(b).

The increase in the natural frequency of the attached resonators promotes discrepancy between the different position configurations. In Fig. 9, the receptance responses obtained with $f = 460$ Hz are depicted. In this case, where there is Bragg-local resonance coupling, the results indicate that the GP in the position of the resonators creates a region of wider vibration (a) and wave (b) attenuation compared to the AP and QP configurations. However, the atten-

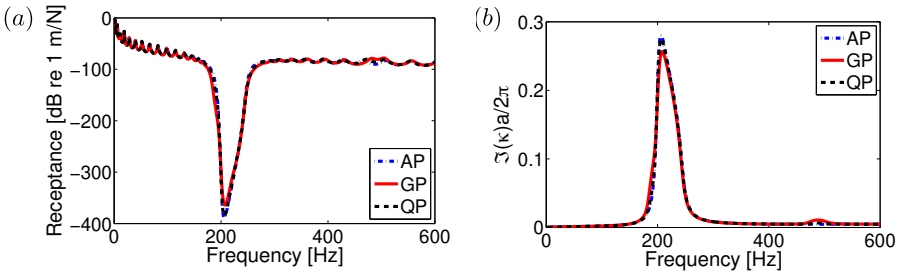

Figure 8: Comparison between AP, GP, and QP (a) receptances and (b) the smallest value of the Bloch vector $\Im(\kappa)a/2\pi$ for the finite graded LR metamaterial beam with $f = 200$ Hz obtained by the WSE.

uation amplitude for the GP configuration is smaller. When resonators are arranged in a AP configuration, i.e., equally spaced, the attenuation amplitude is greater but the frequency range is narrower. In general, the QP configuration produces vibration attenuation with intermediate characteristics, featuring a large attenuation valley and a relatively wide attenuation region.

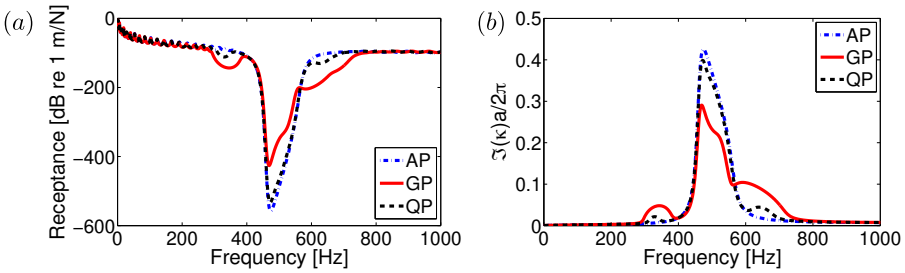

Figure 9: The same as in Fig. 8, but for the natural frequency of resonators $f = 460$ Hz. In this configuration, wave and vibration attenuation is increased due to the coupling of Bragg and local resonance band gaps.

For natural frequencies of resonators higher than the Bragg-resonance coupling, it is possible to observe two attenuation regions corresponding to the Bragg and local resonance band gaps. In Fig. 10, the receptance responses considering $f = 720$ Hz are shown. As in previous cases, the GP configuration presented a greater width of the attenuation region, followed by the QP configuration. In these graded configurations, the attenuation amplitude valley,

Fig. 10(a), and peak, Fig. 10(b), is greater for AP arrays of resonators. In general, the nonuniform (GP and QP) configurations have a greater width of the attenuation region, while AP shows a greater attenuation amplitude.

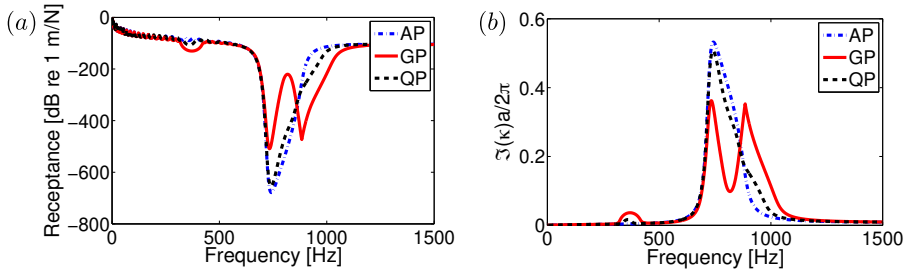

Figure 10: The same as in Figs. 8 and 9, but for the natural frequency of resonators $f = 720$ Hz. In this case, there is no coupling between the Bragg and local resonance band gaps.

3.2. Gradation in the resonator position and attached mass simultaneously

In this section, the simultaneous variation of the position x_j and mass m_j of the resonators in a graded LR metamaterial beam of lattice constant a is considered, as illustrated in Fig. 1.

Therefore, all studied combinations correspond to graded configurations. Specifically, the variation of mass is investigated following the AP, GP and QP configurations, given respectively by the expressions:

$$m_j = \frac{\sigma_r M_c}{N^2} + \overline{d}(j-1), \tag{8}$$

$$m_j = \frac{\sigma_r M_c}{N^2}\overline{r}^{j-1}, \tag{9}$$

$$m_j = \frac{\sigma_r M_c}{N^2} + \overline{\beta}(j-1)^2, \tag{10}$$

with $\overline{d}$, $\overline{r}$, and $\overline{\beta}$ being the respective constants of each progression, obtained through the relationship between the unit cell mass (bared) and the total mass of the resonators attached to it (see Eq. (4)).

The modification in the distribution of the resonators' mass results in changes in the natural vibration frequencies of each resonator. Consequently, introducing gradation into the mass of the resonators is expected to manifest the effect

of local resonance for each resonator's frequency f_j, leading to the formation of new band gaps and regions of vibration attenuation. In the simulations, a set of $N = 10$ resonators with identical elastic constants ($k_1 = \cdots = k_N = k$) is considered. To perform numerical simulations with $\sigma_r = 0.5$, the following constants $\overline{d} = M_c\dfrac{2\sigma_r}{N^2}$, $\overline{r} = 1.4739$, and $\overline{\beta} = M_c\dfrac{6\sigma_r}{19N^2}$ are considered.

For scenarios where the mass gradation adheres to an AP, the resonator masses are specified by Eq. (8), and the natural frequencies of the resonators are $f_{j,\ AP} = \{1455.10, 840.10, 650.74, 549.98, 485.03, 438.73, 403.57, 375.71, 352.91, 333.82\}$ Hz. Unlike the case where only the resonators' position follows an AP, the incorporation of graded effects in the mass distribution of the resonators results in a model with standard periodicity a. Therefore, configurations that follow AP in the resonators' mass distribution, Eq. (8), present the Bragg band gap at the expected frequency f_{Bragg}, Eq. (3).

Conversely, for cases where the mass configuration follows a GP, Eq. (9), the natural frequencies of the resonators are $f_{j,\ GP} = \{1455.10, 1198.54, 987.22, 813.16, 669.79, 551.69, 454.42, 374.30, 308.30, 253.94\}$ Hz. Finally, when the mass gradation follows a QP, Eq. (10), the corresponding natural frequencies are $f_{j,\ QP} = \{1455.10, 1268.52, 967.24, 742.35, 591.45, 487.89, 413.74, 358.50, 315.94, 282.24\}$ Hz.

To structure the analyses, all combinations of position and mass are investigated, being denoted by its respective acronym, with the first and second referring to the position and mass configurations, respectively. For example, GP-QP denotes a graded LR metamaterial beam with resonator positions arranged according to GP, Eq. (6), and the corresponding mass configuration described by QP, Eq. (10).

The most accurate wave modes arising from the complex dispersion diagram for all combinations of the different configurations of resonator positions and masses are shown in Fig. 11. For completeness, the vibration attenuation regions for each configuration are verified through the respective receptances, presented in Fig. 12. In general, the results show that the highest attenuation peaks (Fig. 11) and valleys (Fig. 12) are located near the natural frequencies

of the more massive resonators. In these configurations, the position of the resonators influences the intensity of the attenuation peaks at their respective locations.

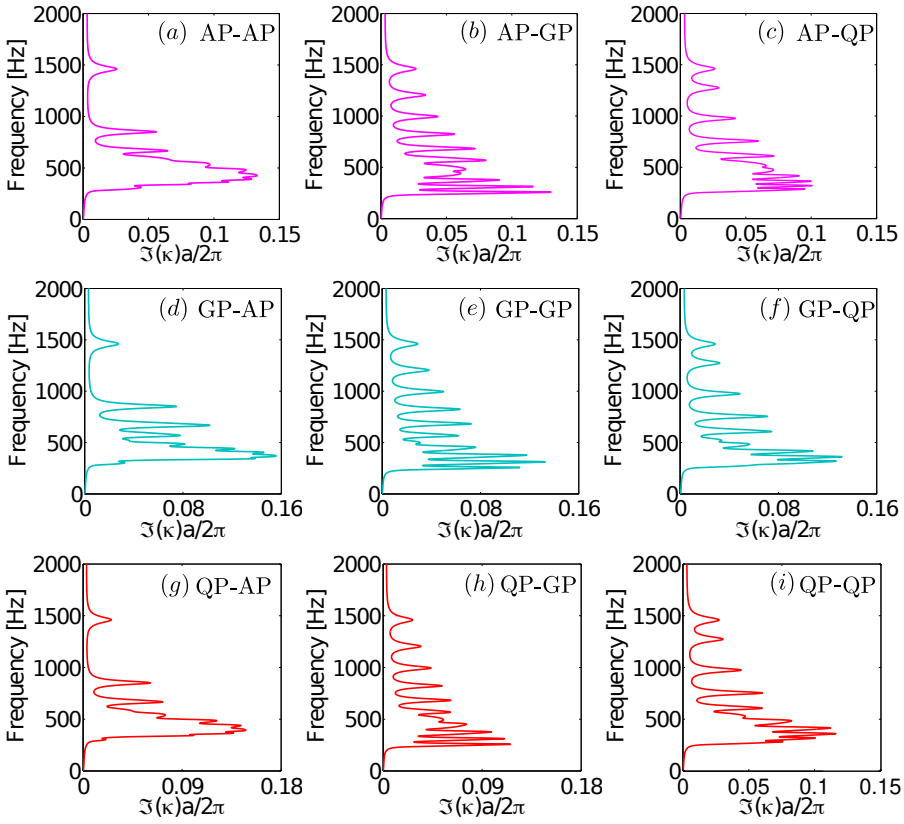

Figure 11: The smallest value of the imaginary part of the Bloch wave vector $\Im(\kappa)a/2\pi$ calculated by the EPWE method for the graded LR metamaterial beam ($N = 10$), considering all position and mass variations of the resonators. The results are obtained by EPWE, accounting for the most accurate modes.

The results in Figs. 11(a-c) and 12(a-c) show significant differences in attenuation when the mass configuration is modified, while maintaining the position of the resonators as in the AP configuration. In these configurations, the vibration and wave attenuation regions for low-frequencies are wider when the mass also has the AP configuration. On the other hand, the lowest frequency

attenuation valley (Fig. 12) is found with the mass graded by the GP structure. For the case of graded LR metamaterial beams with resonators arranged by GP, the different mass configurations promote distinct attenuation peaks and valleys, with the highest attenuation values observed when the masses are arranged in the AP configuration, as shown in Figs. 11(d) and 12(d). Similarly, in Figs. 11(g-i) and 12(g-i), where the resonators position configuration is given by QP, the mass configuration with the greatest attenuation intensity is the AP. The GP-AP combination produces the strongest vibration attenuation valley, followed by the QP-AP configuration, which presents an amplitude similar to the GP-AP case, but with a wider attenuation region.

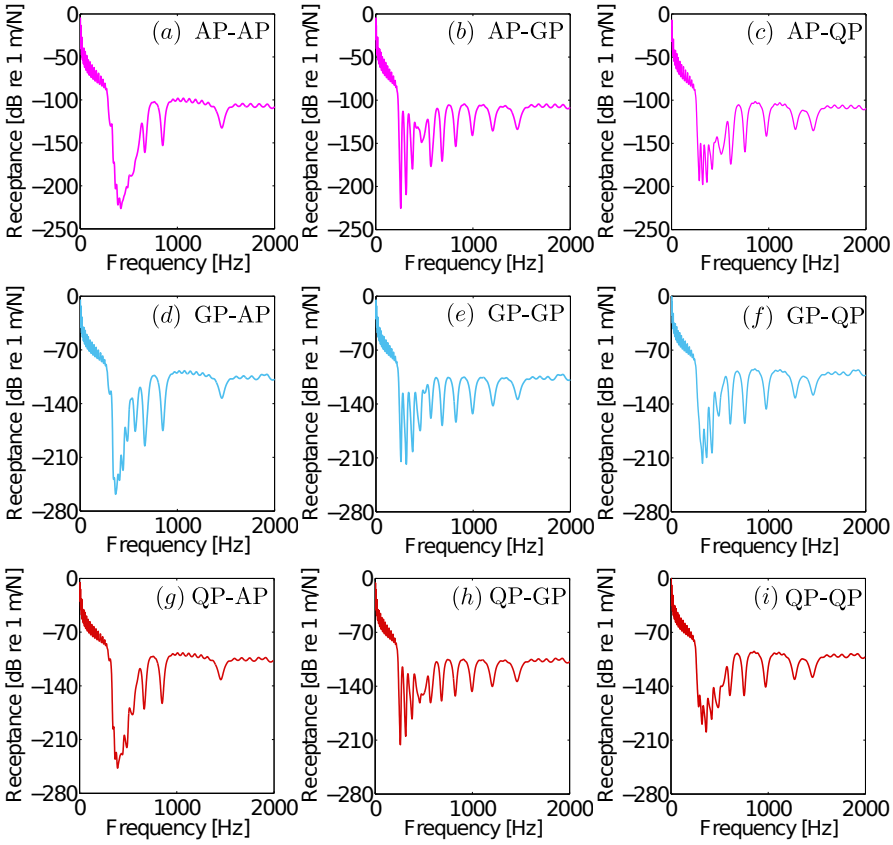

Figure 12: Receptance results for a finite graded LR metamaterial beam composed of 20 unit cells, considering variations in mass and position.

3.3. Influence of the total mass of the resonators on vibration attenuation

In the previous sections, all simulations were conducted considering the total mass of resonators per unit cell fixed at $\sigma_r = 0.5$. In this section, the effects of varying the total mass of the resonators on the region and intensity of wave attenuation are investigated. For this purpose, the lowest values of $|\Im(\kappa)|a/2\pi$ are considered, corresponding to the fourth wave mode (organized by the MAC criterion), for the mass and position configurations AP and QP, obtained by the EPWE method. It is important to note that the lowest value of $|\Im(\kappa)|a/2\pi$ presented by the GP configuration at the position is the overlap of the two wave modes (see Fig. 6(f)). In this case, the results are presented considering the intersection of wave modes one and four. In all simulations, the selected wave modes are the same as those previously presented in Figs. 4, 6 and 7.

Figure 13 presents diagrams showing the lowest value of $|\Im(\kappa)|a/2\pi$ in the plane (frequency, σ_r), considering the gradation in position given by AP, GP, and QP, for an LR metamaterial beam with $N = 10$ resonators of equal masses and natural frequencies of $f = 200$, 460, and 720 Hz. In all analyses, it is observed that increasing the mass of the resonators with respect to the unit cell leads to an increase in unit cell wave attenuation. This effect is known and was observed in previous works, where Euler-Bernoulli [17] and Timoshenko beams [41] where attached spring-mass resonators were considered. In this sense, the analysis of Fig. 13 focuses on the comparison between the regions and amplitudes of unit cell wave attenuation promoted by the different position configurations of the resonators.

Considering the natural frequency $f = 200$ Hz, Fig. 13(a, d, g), the comparison between the different positions of the resonator shows that the AP and QP configurations present more intense wave attenuation, while the GP configuration shows a wider region of wave attenuation. In the cases of the GP and QP configurations, there is an attenuation region near the Bragg frequency f_{Bragg}. Note that the GP configuration presents greater attenuation in the Bragg region than the QP configuration.

For the natural frequency of coupling between the Bragg band gap and the

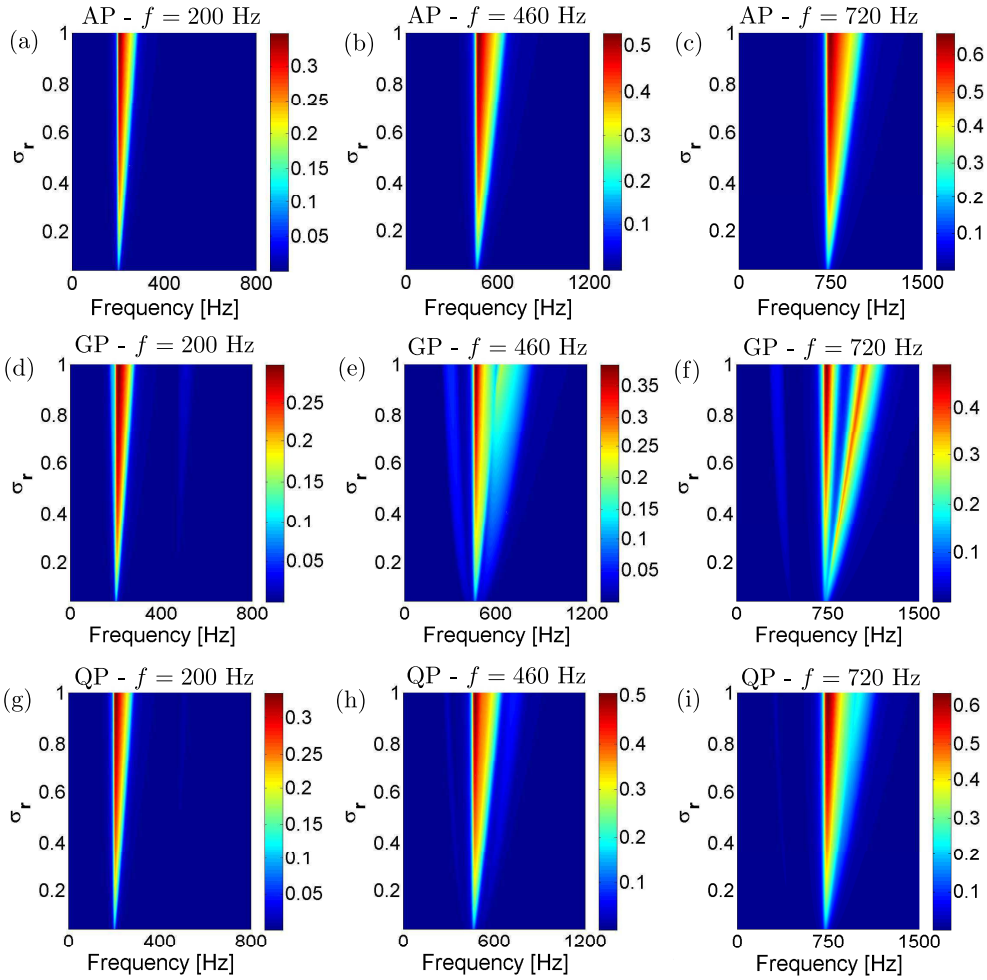

Figure 13: The smallest value of the imaginary part of the Bloch wave vector $|\Im(\kappa)a/2\pi|$ obtained by the EPWE method, considering variations in the total mass of the resonators computed by σ_r. The results are obtained assuming gradation in position for the LR metamaterial beam with equal masses $m = \dfrac{\sigma_r}{N} M_c$.

local resonance, $f = 460$ Hz (Fig. 13(b, e, h)), the gradation in GP presents a very different behavior from the AP and QP cases. The wave attenuation region of the GP exhibits a significantly larger attenuation region compared to the previous cases. In general, coupling promotes an increase in the wave attenuation region and is intensified by the increase in the mass of the resonators.

Increasing σ_r leads to a complete separation of the Bragg and local resonance band gaps for GP (Fig. 13(e)).

For resonator's natural frequency higher than f_{Bragg} (Fig. 13(c, f, i)), the arrangement and intensity of the attenuation regions change for each configuration. Considering $f = 720$ Hz, it is observed that the configurations with the highest intensity, AP and QP, exhibit distinct behaviors with the increase of σ_r, where QP shows a visibly larger and less intense attenuation region compared to AP. The GP configuration shows two well-defined attenuation regions, which increase their respective separations with the increase in the resonator's mass.

It was also evaluated the influence of the parameters $\overline{d}$, $\overline{r}$, and $\overline{\beta}$ of the respective mass grading configurations AP, Eq. (8), GP, Eq. (9), and QP, Eq. (10), on wave attenuation, associated with the variation of the resonator position described by the AP, Eq. (5), GP, Eq. (6), and QP, Eq. (7). The variation of $\overline{d}$, $\overline{r}$, and $\overline{\beta}$ affects the total mass of resonators per unit cell according to each configuration. Therefore, the analysis was restricted to cases with $\sigma_r \leq 1$, where the maximum values of the parameters $\overline{d}$, $\overline{r}$, and $\overline{\beta}$ correspond to the limiting case $\sigma_r = 1$. For comparison purposes, a LR metamaterial beam where all configurations have mass $m_1 = 5.4 \times 10^{-5}$ kg (the same mass m_1 as in Figs. 11 and 12), is considered. Figure 14 shows the comparison between all combinations of position and mass of the resonators, with variation of the parameters $\overline{d}$, $\overline{r}$, and $\overline{\beta}$ related to the mass arrangement of the resonators. As in the previous case, the increase in the mass of the resonators promoted by the increase in $\overline{d}$, $\overline{r}$, and $\overline{\beta}$, leads to greater attenuation intensity.

In the case of AP mass grading (Fig. 14(a)-(c)), it is observed that the wave attenuation region is reduced while the intensity is increased with the increment of $\overline{d}$. In general, the AP-AP configuration shows a slightly wider wave attenuation region than GP-AP and QP-AP. Furthermore, the QP-AP configuration presents the highest attenuation intensity. On the other hand, the GP mass gradation configurations (Fig. 14(d)-(f)) promote the opposite effect, that is, the increase in $\overline{r}$ leads to the widening of the wave attenuation region and also to the increase in the attenuation intensity. Although the configurations are

similar, it is possible to verify that the GP-GP configuration presents a higher attenuation in the f_{Bragg} region, when compared to AP-GP and QP-GP. Finally, the QP mass gradation study is presented in Figs. 14(g)-(i). Different from the previous cases, the attenuation region is slightly affected by the increment of $\overline{\beta}$. The AP-QP configuration shows the largest wave attenuation regions.

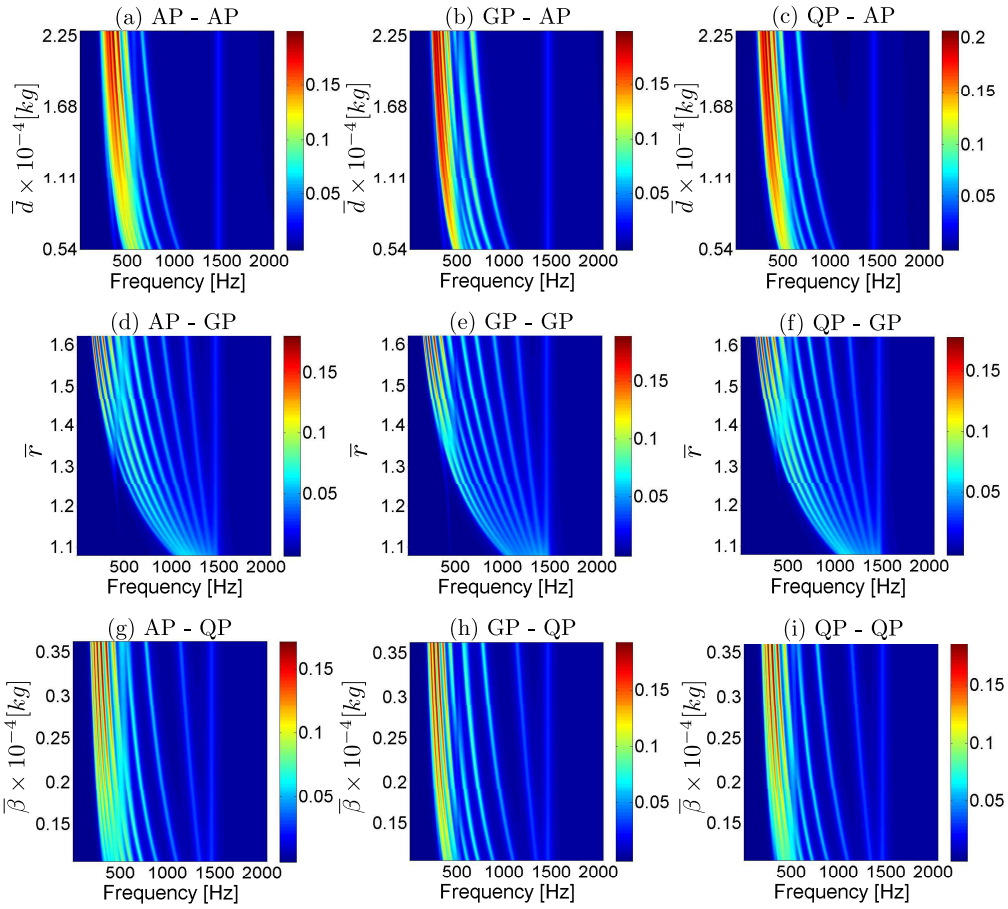

Figure 14: The smallest value of the imaginary part of the Bloch wave vector $|\Im(\kappa)|a/2\pi$ obtained by the EPWE method, taking into account variations in the parameters $\overline{d}$, $\overline{r}$ and $\overline{\beta}$. All results presented were obtained for $\sigma_r \leq 1$, with the maximum values of $\overline{d}$, $\overline{r}$ and $\overline{\beta}$ being relative to $\sigma_r = 1$.

4. Conclusions

In this study, the formation region, intensity and width of the flexural band gaps of a locally resonant graded Euler-Bernoulli beam was investigated. The spatial arrangement and mass of the resonators were characterized in terms of arithmetic, geometric and quadratic progressions. To study the band gaps and the unit cell wave attenuation of the infinite graded locally resonant metamaterial beam, the plane wave expansion, extended plane wave expansion, wave finite element, and wave spectral element methods were applied to compute the dispersion diagrams. To check the vibration attenuation regions and characterize the band gaps, a finite graded locally resonant metamaterial beam was considered, from which the frequency response functions were obtained by exciting the left end of the structure and measuring the transverse displacement at the right opposite end. Two different cases were analyzed. In the first configuration, gradation was considered solely in the position of resonators. In the second case, the gradation was considered simultaneously in mass and position of resonators.

The investigation of the first case shows that the configuration of the position of the resonators has a great influence on the coupling, intensity, and width of the wave and vibration attenuation regions.

- The resonators arranged according to the arithmetic progression produce more intense wave attenuation, while those models arranged via geometric progression present a wider attenuation region. Quadratic progression shows an intermediate dynamic behavior.

- The widening of the wave attenuation region when the natural frequency of the resonators is chosen near the first Bragg band gap, evidencing the existence of coupling between the Bragg and local resonance band gaps.

- Both results are confirmed in the finite structures by the respective frequency response functions calculated via receptance.

In the second configuration, where the gradation occurs both in mass and position, the wave attenuation was investigated through the smallest part of the Bloch wave vector, considering all progression combinations. The influence of the resonator mass on the locally resonant metamaterial beam graded in position was investigated through parametric diagrams.

- The shape of the smallest part of the Bloch wave vector according to the increase in the mass of the attached resonators shows that the increase in the mass leads to both an increase in the intensity and width of the attenuation region.
- Considering gradation in the mass of the resonators, the best dynamic performance in terms of width and depth of the attenuation regions was obtained for the geometric-arithmetic configuration for the resonators' position and mass distribution, respectively.

This work suggests directions for the study of resonant 1-D periodic elastic graded structures and also sheds light on the investigation of attenuation effects produced by different types of gradation in the locally resonant metamaterial beam configuration.

Acknowledgments

The authors thank the Federal Institute of Maranhão (IFMA), Vale Institute of Technology (ITV), and Brazilian funding agencies CAPES (Finance Code 001), CNPq (Grant Reference Numbers 403234/2021-2, 405638/2022-1, 350929/2023-8, and 404417/2024-8), FAPEMA (Grant Reference Numbers BM-07223/22 and BM-03211/24), FAPESP (Grant Reference Number 2018/15894-0), and FADESP.

Appendix A. Plane wave expansion formulation for graded LR metamaterial beam

The PWE method uses the periodicity of the system and the Fourier series expansion in the spatial domain to rewrite the governing equation in terms of an eigenproblem $\omega(\kappa)$, in which elastic bands of purely propagating waves are obtained [78]. In Ref. [17], the authors investigated the propagation of flexural waves in LR metamaterial Euler-Bernoulli beams with multiple mass-spring resonators attached periodically. In this case, the PWE and EPWE formulations were employed to obtain the dispersion diagram, where the band gaps promoted by local resonance were investigated. Here, the PWE formulation is presented as an abbreviated version of Ref. [17], aiming to study the effects of gradation on wave attenuation in graded LR metamaterial beams.

Applying the temporal Fourier transform, Eq. (1) is simplified as

$$EI\frac{\partial^4}{\partial x^4}u(x) - \omega^2\rho S u(x) = \sum_{j=1}^{N}\sum_{n=-\infty}^{+\infty} p_j(x_j + na)\delta[x - (x_j + na)], \qquad (A.1)$$

where $u(x)$ and $p(x)$ are the Fourier transforms of $\hat{u}(x,t)$ and $\hat{p}(x,t)$. For brevity, the frequency (ω) dependence of the variables $u(x) \equiv u(x,\omega)$ and $p(x) \equiv p(x,\omega)$ is omitted. It is worth noting that $p_j(x_j + na)$ is the force experienced by the beam due to the resonator located at position $x_i + na$, with n being an integer. The Dirac delta function, δ, acts in filtering p_j, accounting for the point forces of each resonator. Therefore, the right-hand side of Eq. (A.1) accounts for the external force of the multiple periodic arrays of attached local mass-spring resonators. For resonators with a single DOF, the force applied by the resonator located at $x_j + na$ is given by

$$p_j(x_j + na) = -k_j\left[u(x_j + na) - w_j(x_j + na)\right],\ j = 1,\ 2,\ \ldots,\ N, \qquad (A.2)$$

$$-\omega^2 m_j w_j(x_j + na) = -p_j(x_j + na),\ j = 1,\ 2,\ \ldots,\ N, \qquad (A.3)$$

where $w_j(x_j + na)$ is the displacement of the mass of jth resonator.

In order to rewrite the governing equations of the system in terms of an eigenproblem, the Bloch wave function is expanded in terms of the Fourier

series, resulting in the transverse displacement in the reciprocal space:

$$u(x) = \sum_{\bar{m}=-\infty}^{+\infty} U_{\bar{m}} e^{-i(\kappa+2\pi\bar{m}/a)x}, \tag{A.4}$$

where $2\pi\bar{m}/a$ is the reciprocal lattice vector with $\bar{m} \in \mathbb{Z}$. Furthermore, the localized displacement $u(x_j)$ and the delta function δ are expanded as:

$$u(x_j) = \sum_{m=-\infty}^{+\infty} U_m e^{-i(\kappa+2\pi m/a)x_j}, \tag{A.5}$$

with $m \in \mathbb{Z}$, and

$$\sum_{n=-\infty}^{+\infty} \delta[x - (x_j + na)] = \frac{1}{a} \sum_{m=-\infty}^{+\infty} e^{i(2\pi m/a)x_j} e^{-i(2\pi m/a)x}. \tag{A.6}$$

To obtain the solution of the governing equations, the infinite series in Eqs. (A.4)-(A.6) are truncated at $m, \bar{m} = [-M, \ldots, M]$, where M is an integer. The convergence of the solutions must be checked subsequently, where the choice of M is made. In general, the convergence of the solutions of plane waves for the LR metamaterial beam model occurs for small values of M [17, 41]. We highlight that no regularization was used for the PWE method, since the number of plane waves used in this article (i.e., 3) is suitable for the Fourier convergence in cases of 1-D and 2-D mechanical metamaterials with attached spring-mass resonators [41].

By substituting the truncated series into Eqs. (A.1)-(A.3), an eigenproblem can be obtained as:

$$\Big[\boldsymbol{Q} - \omega^2 \mathbf{N}\Big]\boldsymbol{B} = \mathbf{0}, \tag{A.7}$$

where

$$\boldsymbol{Q} = \begin{bmatrix} aEI\boldsymbol{\mathcal{K}} + \sum_{j=1}^{N} k_j \boldsymbol{S_j}\overline{\boldsymbol{S}}_{\boldsymbol{j}} & -k_1\boldsymbol{S_1} & -k_2\boldsymbol{S_2} & \ldots & -k_N\boldsymbol{S_N} \\ -k_1\overline{\boldsymbol{S}}_{\boldsymbol{1}} & k_1 & 0 & \ldots & 0 \\ -k_2\overline{\boldsymbol{S}}_{\boldsymbol{2}} & 0 & k_2 & \vdots & \vdots \\ \vdots & \vdots & \ldots & \ddots & 0 \\ -k_N\overline{\boldsymbol{S}}_{\boldsymbol{N}} & 0 & \ldots & 0 & k_N \end{bmatrix}, \tag{A.8}$$

$$\boldsymbol{N} = \begin{bmatrix} a\rho S\mathbf{I} & \mathbf{0} & \mathbf{0} & \dots & \mathbf{0} \\ \mathbf{0} & m_1 & 0 & \dots & 0 \\ \mathbf{0} & 0 & m_2 & \vdots & \vdots \\ \mathbf{0} & \vdots & \dots & \ddots & 0 \\ \mathbf{0} & 0 & \dots & 0 & m_N \end{bmatrix}, \quad \boldsymbol{B} = \begin{bmatrix} \boldsymbol{U} \\ w_1 \\ w_2 \\ \vdots \\ w_N \end{bmatrix}, \tag{A.9}$$

with

$$\mathbf{I} = \begin{bmatrix} 1 & 0 & \dots & 0 \\ 0 & 1 & \dots & 0 \\ \vdots & 0 & \ddots & \vdots \\ 0 & \vdots & \dots & 1 \end{bmatrix}_{M\times M} \quad \text{and} \quad \boldsymbol{U} = \begin{bmatrix} U_{-M} \\ U_{-M+1} \\ \vdots \\ U_M \end{bmatrix}. \tag{A.10}$$

The matrices $\boldsymbol{\mathcal{K}}$, $\boldsymbol{S_j}$ and $\overline{\boldsymbol{S}}_{\boldsymbol{j}}$ are given by

$$\boldsymbol{\mathcal{K}} = \begin{bmatrix} [\kappa - 2\pi M/a]^4 & 0 & \dots & 0 \\ 0 & [\kappa - 2\pi(M-1)/a]^4 & \vdots & \vdots \\ \vdots & \dots & \ddots & 0 \\ 0 & \dots & \dots & [\kappa + 2\pi M/a]^4 \end{bmatrix}, \tag{A.11}$$

$$\overline{\boldsymbol{S}}_{\boldsymbol{j}}^{\mathrm{T}} = \begin{bmatrix} e^{-i[\kappa-2\pi M/a]x_j} \\ e^{-i[\kappa-2\pi(M-1)/a]x_j} \\ \vdots \\ e^{-i[\kappa+2\pi M/a]x_j} \end{bmatrix} \text{and} \quad \boldsymbol{S_j} = \begin{bmatrix} e^{i[\kappa-2\pi M/a]x_j} \\ e^{i[\kappa-2\pi(M-1)/a]x_j} \\ \vdots \\ e^{i[\kappa+2\pi M/a]x_j} \end{bmatrix}. \tag{A.12}$$

Equation (A.7) represents the generalized eigenvalue problem $\omega(\kappa)$ arising from the PWE formulation. For each Bloch wave vector κ, $2M+1+N$ eigenvalues ω^2 are obtained.

Appendix B. Extended plane wave expansion formulation for graded LR metamaterial beam

To study the behavior of evanescent waves, the EPWE method, $\kappa(\omega)$, is applied. In this approach, the Bloch wave vector takes complex values, enabling

an effective investigation into the attenuation of waves via complex dispersion diagrams [74–77]. For the study of evanescent waves, standard structural damping of the graded LR metamaterial beams can be considered. Here, the beam damping due to the material through the complex Young's modulus is considered, i.e. $E \to E(1+i\eta_{\rm b})$, and the damping arising from the resonators induced by the spring constant $k_j \to k_j(1+i\eta_{\rm r})$.

The EPWE formulation is performed by substituting Eqs. (A.4)-(A.6) in model (A.1), which results in the expression:

$$[aEI(\kappa+2\bar{m}\pi/a)^4 - a\omega^2\rho S]U_{\bar{m}} + \sum_{j=1}^{N}\sum_{m=-\infty}^{\infty}\gamma_j e^{i(2\bar{m}\pi/a)x_j}e^{-i(2m\pi/a)x_j}U_m = 0, \tag{B.1}$$

where $\gamma_j = \dfrac{-m_j\omega^2}{1-\omega^2[\overline{\omega}_j^2(1+i\eta_r)]^{-1}}$, with $\overline{\omega}_j = \sqrt{k_j/m_j} = 2\pi f_j$ being the frequency of jth resonator. After some algebraic manipulations, Eq. (B.1) is rewritten in a matrix form as:

$$\begin{bmatrix} -\boldsymbol{C_3} & -\boldsymbol{C_2} & -\boldsymbol{C_1} & -\boldsymbol{C_0} \\ \mathbf{I} & \mathbf{0} & \mathbf{0} & \mathbf{0} \\ \mathbf{0} & \mathbf{I} & \mathbf{0} & \mathbf{0} \\ \mathbf{0} & \mathbf{0} & \mathbf{I} & \mathbf{0} \end{bmatrix} \begin{bmatrix} \bar{\kappa}^3\boldsymbol{U} \\ \bar{\kappa}^2\boldsymbol{U} \\ \bar{\kappa}\boldsymbol{U} \\ \boldsymbol{U} \end{bmatrix} = \bar{\kappa} \begin{bmatrix} \bar{\kappa}^3\boldsymbol{U} \\ \bar{\kappa}^2\boldsymbol{U} \\ \bar{\kappa}\boldsymbol{U} \\ \boldsymbol{U} \end{bmatrix}, \tag{B.2}$$

where $\bar{\kappa} = a\kappa$, $\boldsymbol{C}_{1,2,3} = \boldsymbol{\Gamma}_{1,2,3}$, and $\boldsymbol{C}_0 = \boldsymbol{\Gamma}_0 + \sum_{j=1}^{N}\dfrac{a^3\gamma_j}{EI}\boldsymbol{P}_j\overline{\boldsymbol{P}}_j - \dfrac{\rho S a^4\omega^2}{EI}\mathbf{I}$, with $\beta_0(n) = 16(\pi n)^4$, $\beta_1(n) = -32(\pi n)^3$, $\beta_2(n) = 24(\pi n)^2$, $\beta_3(n) = -8\pi n$,

$$\boldsymbol{\Gamma}_{j=0,1,2,3} = \begin{bmatrix} \beta_j(-M) & 0 & \dots & 0 \\ 0 & \beta_j(-M+1) & \vdots & \vdots \\ \vdots & \dots & \ddots & 0 \\ 0 & \dots & \dots & \beta_j(M) \end{bmatrix}, \tag{B.3}$$

$$\boldsymbol{P}_j^{\rm T} = \begin{bmatrix} e^{-i[\kappa-2\pi M/a]x_j} & e^{-i[\kappa-2\pi(M-1)/a]x_j} & \dots & e^{-i[\kappa+2\pi M/a]x_j} \end{bmatrix}, \tag{B.4}$$

and

$$\overline{\boldsymbol{P}}_j = \begin{bmatrix} e^{i[\kappa-2\pi M/a]x_j} & e^{i[\kappa-2\pi(M-1)/a]x_j} & \dots & e^{i[\kappa+2\pi M/a]x_j} \end{bmatrix}. \tag{B.5}$$

The eigenvalue problem (B.2) represents the EPWE formulation, $\kappa(\omega)$, for the graded LR metamaterial beam. For a given angular frequency ω, $4(2M+1)$ eigenvalues $\bar{\kappa}$ are found.

Appendix C. Wave finite element formulation for graded LR metamaterial beam

The WFE method is applied to analyze a 1-D graded MM Euler-Bernoulli beam. Within the finite element (FE) framework, a single cell may be viewed itself as a periodic structure, providing that it is meshed periodically in the direction of propagation. The full structure is therefore equivalent to an assembly of N_c identical substructures having the same number of DOFs, n, on their left and right edges, as shown, for example, in Fig. 1.

The WFE method uses the dynamic stiffness matrix $\mathbf{D} = \mathbf{K} - \omega^2\mathbf{M}$ of the unit cell, where $\mathbf{K}$ and $\mathbf{M}$ are respectively the stiffness and mass matrices of this cell, built from the classical Euler-Bernoulli beam theory.

The dynamic equilibrium equation of the substructure is then

$$\mathbf{D}\mathbf{u} = \mathbf{F}, \tag{C.1}$$

where $\mathbf{u}$ and $\mathbf{F}$ are respectively the vectors of DOFs and forces applied to the substructure. Assuming that there are no internal forces and partitioning the DOFs between the left and right edges and the internal domain of the substructure, Eq. (C.1) may be rewritten as follows:

$$\begin{bmatrix} \mathbf{D}_{ii} & \mathbf{D}_{il} & \mathbf{D}_{ir} \\ \mathbf{D}_{li} & \mathbf{D}_{ll} & \mathbf{D}_{lr} \\ \mathbf{D}_{ri} & \mathbf{D}_{rl} & \mathbf{D}_{rr} \end{bmatrix} \begin{Bmatrix} \mathbf{u}_i \\ \mathbf{u}_l \\ \mathbf{u}_r \end{Bmatrix} = \begin{Bmatrix} \mathbf{0} \\ \mathbf{F}_l \\ \mathbf{F}_r \end{Bmatrix}. \tag{C.2}$$

Expressing the internal DOFs as:

$$\mathbf{u}_i = \mathbf{D}_{ii}^{-1}(\mathbf{D}_{il}\mathbf{u}_l + \mathbf{D}_{ir}\mathbf{u}_r), \tag{C.3}$$

Equation (C.2) may be condensed in the following form:

$$\begin{bmatrix} \mathbf{D}_{ll}^{*} & \mathbf{D}_{lr}^{*} \\ \mathbf{D}_{rl}^{*} & \mathbf{D}_{rr}^{*} \end{bmatrix} \begin{Bmatrix} \mathbf{u}_l \\ \mathbf{u}_r \end{Bmatrix} = \begin{Bmatrix} \mathbf{F}_l \\ \mathbf{F}_r \end{Bmatrix}, \tag{C.4}$$

where the terms of the condensed dynamic stiffness $\mathbf{D}^*$ are respectively defined as $\mathbf{D}^*_{ll} = \mathbf{D}_{ll} - \mathbf{D}_{li}\mathbf{D}_{ii}^{-1}\mathbf{D}_{il}$, $\mathbf{D}^*_{rl} = \mathbf{D}_{rl} - \mathbf{D}_{ri}\mathbf{D}_{ii}^{-1}\mathbf{D}_{il}$, $\mathbf{D}^*_{lr} = \mathbf{D}_{lr} - \mathbf{D}_{li}\mathbf{D}_{ii}^{-1}\mathbf{D}_{ir}$, and $\mathbf{D}^*_{rr} = \mathbf{D}_{rr} - \mathbf{D}_{ri}\mathbf{D}_{ii}^{-1}\mathbf{D}_{ir}$.

Equation (C.4) may finally be rearranged in a state vector form:

$$\underbrace{\begin{Bmatrix} \mathbf{u}_r \\ \mathbf{F}_r \end{Bmatrix}}_{\mathbf{q}_r} = \underbrace{\begin{bmatrix} -{\mathbf{D}^*_{lr}}^{-1}\mathbf{D}^*_{ll} & -{\mathbf{D}^*_{lr}}^{-1} \\ \mathbf{D}^*_{rl} - \mathbf{D}^*_{rr}{\mathbf{D}^*_{lr}}^{-1}\mathbf{D}^*_{ll} & -\mathbf{D}^*_{rr}{\mathbf{D}^*_{lr}}^{-1} \end{bmatrix}}_{\mathbf{T}} \underbrace{\begin{Bmatrix} \mathbf{u}_l \\ -\mathbf{F}_l \end{Bmatrix}}_{\mathbf{q}_l}, \tag{C.5}$$

where $\mathbf{T}$ is the transfer matrix that relates the left state vector $\mathbf{q}_l$ to the right state vector $\mathbf{q}_r$ of the unit cell.

Appendix C.1. Local periodicity condition

Let's now consider two consecutive unit cells, numbered respectively m and $m+1$, within a single beam. The displacement continuity condition ${\mathbf{u}_r}^{(m)} = {\mathbf{u}_l}^{(m+1)}$ and the force balance ${\mathbf{F}_r}^{(m)} = -{\mathbf{F}_l}^{(m+1)}$ produce the condition ${\mathbf{q}_r}^{(m)} = {\mathbf{q}_l}^{(m+1)}$. Substituting this relation in Eq. (C.5), the following condition is obtained

$${\mathbf{q}_l}^{(m+1)} = \mathbf{T}{\mathbf{q}_l}^{(m)}. \tag{C.6}$$

The Floquet-Bloch's theorem for wave propagation in an infinite periodic system [86] (Eq. 2) applied to consecutive substructures can be rewrite as

$$\begin{aligned} \mathbf{u}_l^{(m+1)} &= e^{\mu}\,\mathbf{u}_l^{(m)}, \\ \mathbf{F}_l^{(m+1)} &= -e^{\mu}\,\mathbf{F}_l^{(m)}, \end{aligned} \tag{C.7}$$

where $\mu = -\Re\{i\kappa\}\mathrm{a}$ is the unit cell attenuation constant obtained via WFE [17]. The periodic condition (Eq. C.6) may therefore be finally written as:

$$\mathbf{T}\mathbf{q}_l = e^{\mu}\,\mathbf{q}_l. \tag{C.8}$$

However, even if the matrix $\mathbf{D}^*_{lr}$ from Eq. (C.5) is invertible, numerical ill-conditioning in $\mathbf{T}$ is likely to occur. To avoid this issue, a representation by displacement/rotation vector alone is preferable [87]. By rewriting the state

vectors as functions of the left and right displacement/rotation vectors:

$$\mathbf{q}_l = \underbrace{\begin{bmatrix} \mathbf{I}_n & \mathbf{0} \\ -\mathbf{D}^*_{ll} & -\mathbf{D}^*_{lr} \end{bmatrix}}_{\mathbf{L_T}} \underbrace{\begin{Bmatrix} \mathbf{u}_l \\ \mathbf{u}_r \end{Bmatrix}}_{\mathbf{w}} \quad \text{and} \quad \mathbf{q}_r = \underbrace{\begin{bmatrix} \mathbf{0} & \mathbf{I}_n \\ \mathbf{D}^*_{rl} & \mathbf{D}^*_{rr} \end{bmatrix}}_{\mathbf{N_T}} \underbrace{\begin{Bmatrix} \mathbf{u}_l \\ \mathbf{u}_r \end{Bmatrix}}_{\mathbf{w}}, \tag{C.9}$$

the transfer matrix can be expressed as $\mathbf{T} = \mathbf{N_T}\mathbf{L_T^{-1}}$, where the matrices $\mathbf{L_T}$ and $\mathbf{N_T}$ are invertible if $\mathbf{D}^*_{lr}$ is invertible. Thus, Eq. (C.8) leads to the generalized eigenequation

$$e^{\mu}\mathbf{L_T}\mathbf{w} = \mathbf{N_T}\mathbf{w}, \tag{C.10}$$

admitting $2n$ eigenvalues e^{μ_j} and eigenvectors $\mathbf{w}_j$. The eigenvectors of the initial problem, Eq. (C.8), are then computed as $\mathbf{\Phi}_j = \mathbf{L_T}\mathbf{w}_j$. In the above equations, κ_j represents the wave number, and $\mathbf{\Phi}_j$ the corresponding wave mode. It can also be shown that the eigenvalues come in pairs $\{e^{\mu_j}, e^{\mu_j^\star}\}$ for $j = 1, \dots n$, with $e^{\mu_j^\star} = 1/e^{\mu_j}$; the first set of eigenvalues verify the property $|e^{\mu_j}| \leq 1$ and correspond to waves traveling towards the right direction, while for the second set $|e^{\mu_j^\star}| \geq 1$, which corresponds to waves traveling towards the left direction. The corresponding eigenvectors are denoted respectively as $\mathbf{\Phi}_j$ and $\mathbf{\Phi}^\star_j$, $j = 1, \dots, n$. Defining matrices $\boldsymbol{\mu} = \text{diag}\{e^{\mu_j}\}_{j=1,\dots,n}$, $\boldsymbol{\mu}^\star = \text{diag}\{e^{\mu_j^\star}\}_{j=1,\dots,n}$, $\mathbf{\Phi} = \{\mathbf{\Phi}_j\}_{j=1,\dots,n}$ and $\mathbf{\Phi}^\star = \{\mathbf{\Phi}^\star_j\}_{j=1,\dots,n}$, the state vector $\mathbf{q}_l^{(m)}$ of the mth unit cell can be finally expressed as [88]:

$$\mathbf{q}_l^{(m)} = \mathbf{\Phi}\ \mathbf{u}^{(m)} + \mathbf{\Phi}^\star\ \mathbf{u}^{\star\,(m)}, \quad m = 1 \dots N_c + 1, \tag{C.11}$$

where $\mathbf{u}^{(m)}$ and $\mathbf{u}^{\star\ (m)}$ are the $n \times 1$ vectors of wave amplitudes at the left boundary of the mth unit cell and depend on the boundary conditions at the extremities of the whole structure. They satisfy the following properties: $\mathbf{u}^{(m+1)} = \boldsymbol{\mu}\mathbf{u}^{(m)}$ and $\mathbf{u}^{\star\,(m)} = \boldsymbol{\mu}\mathbf{u}^{\star\,(m+1)}$. Defining the amplitude vectors $\mathbf{u} = \mathbf{u}^{(1)}$ and $\mathbf{u}^\star = \mathbf{u}^{\star\,(N_c+1)}$ at the extremities of a beam (N_c being the number of unit cells composing the beam), Eq. (C.11) may be rewritten as follows:

$$\mathbf{q}_l^{(m)} = \mathbf{\Phi}\,\boldsymbol{\mu}^{m-1}\,\mathbf{u} + \mathbf{\Phi}^\star\,\boldsymbol{\mu}^{N_c+1-m}\,\mathbf{u}^\star, \quad m = 1 \dots N_c + 1. \tag{C.12}$$

For a beam with prescribed boundary conditions, the unknown amplitude

vectors $\mathbf{u}$ and $\mathbf{u}^\star$ are computed by solving a matrix system that expresses the boundary conditions in matrix form. As an illustration, the case of a free-free beam which is subject to a force vector $\mathbf{F}_L$ on its left end and $\mathbf{F}_R$ on its right end is considered. Further partitioning the eigenvector matrices as $\mathbf{\Phi} = \left[\mathbf{\Phi}_{\rm F}^T \; \mathbf{\Phi}_{\rm F}^T\right]^T$ and $\mathbf{\Phi}^\star = \left[\mathbf{\Phi}_{\rm F}^{\star T} \; \mathbf{\Phi}_{\rm F}^T\right]^{\star T}$, the boundary conditions may be written as

$$\mathbf{\Phi}_{\rm F}\,\mathbf{u} + \mathbf{\Phi}_{\rm F}^\star\,\boldsymbol{\mu}^N\,\mathbf{u}^\star = -\mathbf{F}_L, \tag{C.13}$$

$$\mathbf{\Phi}_{\rm F}\,\boldsymbol{\mu}^N\,\mathbf{u} + \mathbf{\Phi}_{\rm F}^\star\,\mathbf{u}^\star = \mathbf{F}_R. \tag{C.14}$$

The computation of $\mathbf{u}$ and $\mathbf{u}^\star$ follows from the inversion of the resulting matrix system

$$\begin{bmatrix} \mathbf{I}_n & \mathbf{\Phi}_{\rm F}^{-1}\,\mathbf{\Phi}_{\rm F}^\star\boldsymbol{\mu}^N \\ \mathbf{\Phi}_{\rm F}^{\star\,-1}\,\mathbf{\Phi}_{\rm F}\,\boldsymbol{\mu}^N & \mathbf{I}_n \end{bmatrix} \begin{bmatrix} \mathbf{u} \\ \mathbf{u}^\star \end{bmatrix} = \begin{bmatrix} -\mathbf{\Phi}_{\rm F}^{-1}\,\mathbf{F}_L \\ \mathbf{\Phi}_{\rm F}^{\star\,-1}\,\mathbf{F}_R \end{bmatrix}, \tag{C.15}$$

where $\mathbf{I}_n$ is the identity matrix of rank n.

Appendix D. Wave spectral element formulation for graded LR metamaterial beam

The wave spectral element (WSE) method is an advanced technique for analyzing the dynamic response of structures. This method combines the advantages of the spectral element (SE) and FE methods, allowing for a precise representation of wave propagation in complex systems.

Appendix D.1. Dynamic stiffness for beams

The WSE formulation follows the same procedure as for the WFE method, with the difference in the assemble of the dynamic stiffness matrix and the advantage of obtaining analytic solutions for the wave propagation problem [79]. The dynamic stiffness matrix,

$$\tilde{\mathbf{D}} = \begin{bmatrix} \hat{k}_{11} & \hat{k}_{12} & \hat{k}_{13} & \hat{k}_{14} \\ \hat{k}_{21} & \hat{k}_{22} & \hat{k}_{23} & \hat{k}_{24} \\ \hat{k}_{31} & \hat{k}_{32} & \hat{k}_{33} & \hat{k}_{34} \\ \hat{k}_{41} & \hat{k}_{42} & \hat{k}_{43} & \hat{k}_{44} \end{bmatrix}, \tag{D.1}$$

resulting from the WSE allows the incorporation of dynamic effects in the beam behavior. The individual stiffness terms of the matrix $\tilde{\mathbf{D}}$ are:

$$
\begin{aligned}
\hat{k}_{11} &= \frac{(\kappa_2^2 - \kappa_1^2)(r_1 z_{22} + r_2 z_{21})}{\Delta}, \\
\hat{k}_{13} &= \frac{(\kappa_1^2 - \kappa_2^2)(r_1 z_{21} + r_2 z_{22})}{\Delta}, \\
\hat{k}_{12} &= \frac{[-i\kappa_2(r_1 z_{11} + r_2 z_{12}) + i\kappa_1(r_1 z_{11} - r_2 z_{12})]}{\Delta}, \\
\hat{k}_{14} &= \frac{[-i\kappa_1(r_1 z_{12} - r_2 z_{11}) - i\kappa_2(r_1 z_{12} + r_2 z_{11})]}{\Delta}, \\
\hat{k}_{22} &= \frac{(-i\kappa_1 R_2 + i\kappa_2 R_1)(r_1 z_{22} - r_2 z_{21})}{\Delta}, \\
\hat{k}_{24} &= \frac{(i\kappa_1 R_2 - i\kappa_2 R_1)(r_1 z_{21} - r_{22} z_4)}{\Delta}, \\
\hat{k}_{23} &= -\hat{k}_{14}, \quad \hat{k}_{33} = \hat{k}_{11}, \quad \hat{k}_{34} = -\hat{k}_{12}, \quad \hat{k}_{44} = \hat{k}_{22},
\end{aligned}
\tag{D.2}
$$

the terms are defined as follows,

$$
\begin{aligned}
r_1 &= (R_1 - R_2) z_{11}, \\
r_2 &= (R_1 + R_2) z_{12}, \\
\Delta &= \frac{(r_1^2 - r_2^2)}{EI},
\end{aligned}
\tag{D.3}
$$

$$
\begin{aligned}
z_{11} &= 1 - e^{-i\kappa_1 a} e^{-i\kappa_2 a}, \\
z_{22} &= 1 + e^{-i\kappa_1 a} e^{-i\kappa_2 a}, \\
z_{12} &= e^{-i\kappa_1 a} - e^{-i\kappa_2 a}, \\
z_{21} &= e^{-i\kappa_1 a} + e^{-i\kappa_2 a}.
\end{aligned}
\tag{D.4}
$$

Here, a is the length of the beam element. R_1 and R_2 are parameters related to the boundary conditions and properties of the beam element, and are given by

$$
R_i = \frac{i\kappa_i G S K_1}{G S K_1 \kappa_i^2 - \rho S \omega^2},
\tag{D.5}
$$

where κ_i are the wave numbers, G is the shear modulus, and K_1 is a parameter related to the stiffness of the element.

References

[1] T.-C. Lim, 2D metamaterial with in-plane positive and negative thermal expansion and thermal shearing based on interconnected alternating bi-materials, Materials Research Express 6 (2019) 115804. doi:10.1088/2053-1591/ab4846.

[2] Q. Zhang, Y. Sun, Novel metamaterial structures with negative thermal expansion and tunable mechanical properties, International Journal of Mechanical Sciences 261 (2024) 108692. doi:10.1016/j.ijmecsci.2023.108692.

[3] H. Wang, Y. Zhang, W. Lin, Q.-H. Qin, A novel two-dimensional mechanical metamaterial with negative poisson's ratio, Computational Materials Science 171 (2020) 109232. doi:10.1016/j.commatsci.2019.109232.

[4] M. Shaat, A. Wagih, Hinged-3D metamaterials with giant and strain-independent poisson's ratios, Scientific Reports 10 (2020) 2228. doi:10.1038/s41598-020-59205-x.

[5] Y. Pan, Y. Zhou, Q. Gao, B. Sun, A novel 3D polygonal double-negative mechanical metamaterial with negative stiffness and negative poisson's ratio, Composite Structures 331 (2024) 117878. doi:10.1016/j.compstruct.2024.117878.

[6] L. Wu, Y. Wang, K. Chuang, F. Wu, Q. Wang, W. Lin, H. Jiang, A brief review of dynamic mechanical metamaterials for mechanical energy manipulation, Materials Today 44 (2021) 168–193. doi:10.1016/j.mattod.2020.10.006.

[7] R. Craster, S. Guenneau, M. Kadic, M. Wegener, Mechanical metamaterials, Reports on Progress in Physics 86 (2023). doi:10.1088/1361-6633/ace069.

[8] P. Jiao, J. Mueller, J. R. Raney, X. R. Zheng, A. H. Alavi, Mechanical metamaterials and beyond, Nature Communications 14 (2023). doi:10.1038/s41467-023-41679-8.

[9] J. Lee, Y. Y. Kim, Elastic metamaterials for guided waves: from fundamentals to applications (2023). doi:10.1088/1361-665X/ad0393.

[10] Y. Jin, D. Torrent, B. D. Rouhani, L. He, Y. Xiang, F.-Z. Xuan, Z. Gu, H. Xue, J. Zhu, Q. Wu, G. Huang, P. D. García, G. Arregui, Y. Chen, S. Guenneau, M. Wegener, M. Kadic, Y. Liu, J. Li, Y.-S. Wang, A. Palermo, V. Romero-García, S. Kuznetsova, E. Cheron, M. L. Navarro, J.-P. Groby, V. Pagneux, S. Félix, L. M. Garcia-Raffi, G. Hu, R. Cai, T. Rabczuk, X. Zhuang, P. Gao, Y. Qu, M. I. Hussein, M. Nomura, Y. Pennec, F. Cai, X. Li, W. Zhai, The 2024 phononic crystals roadmap, Journal of Physics D: Applied Physics 58 (2025) 113001. doi:10.1088/1361-6463/ad9ab2.

[11] V. Laude, Y. Achaoui, S. Benchabane, A. Khelif, Evanescent bloch waves and the complex band structure of phononic crystals, Phys. Rev. B 80 (2009) 092301. doi:10.1103/PhysRevB.80.092301.

[12] B. S. Lazarov, J. S. Jensen, Low-frequency band gaps in chains with attached non-linear oscillators, International Journal of Non-Linear Mechanics 42 (2007) 1186–1193. doi:10.1016/j.ijnonlinmec.2007.09.007.

[13] C. Sugino, S. Leadenham, M. Ruzzene, A. Erturk, On the mechanism of bandgap formation in locally resonant finite elastic metamaterials, Journal of Applied Physics 120 (2016). doi:10.1063/1.4963648.

[14] C. Sugino, Y. Xia, S. Leadenham, M. Ruzzene, A. Erturk, A general theory for bandgap estimation in locally resonant metastructures, Journal of Sound and Vibration 406 (2017) 104–123. doi:10.1016/j.jsv.2017.06.004.

[15] K. M. Ho, C. K. Cheng, Z. Yang, X. X. Zhang, P. Sheng, Broadband locally

resonant sonic shields, Applied Physics Letters 83 (26) (2003) 5566–5568. doi:10.1063/1.1637152.

[16] J. C. Hsu, T. T. Wu, Plate waves in locally resonant sonic materials, Japanese Journal of Applied Physics 49 (07HB11) (2010) 1–5. doi:10.1143/JJAP.49.07HB11.

[17] Y. Xiao, J. Wen, X. Wen, Broadband locally resonant beams containing multiple periodic arrays of attached resonators, Physics Letters A 376 (16) (2012) 1384–1390. doi:10.1016/j.physleta.2012.02.059.

[18] Y. Achaoui, V. Laude, S. Benchabane, A. Khelif, Local resonances in phononic crystals and in random arrangements of pillars on a surface, Journal of Applied Physics 114 (104503) (2013) 1–4. doi:10.1063/1.4820928.

[19] A. O. Krushynska, V. G. Kouznetsova, M. G. D. Geers, Towards optimal design of locally resonant acoustic metamaterials, Journal of the Mechanics and Physics of Solids 71 (2014) 179–196. doi:10.1016/j.jmps.2014.07.004.

[20] F. Casadei, K. Bertoldi, Wave propagation in beams with periodic arrays of airfoil-shaped resonating units, Journal of Sound and Vibration 333 (24) (2014) 6532–6547. doi:10.1016/j.jsv.2014.07.008.

[21] G. Hu, L. Tang, R. Das, S. Gao, H. Liu, Acoustic metamaterials with coupled local resonators for broadband vibration suppression, AIP Advances 7 (025211) (2017) 1–13. doi:10.1063/1.4977559.

[22] L. H. Ribeiro, V. F. D. Poggetto, C. Claeys, D. Chronopoulos, J. R. Arruda, Computing dispersion diagrams and forced responses of arbitrarily varying waveguides, International Journal of Mechanical Sciences 258 (2023). doi:10.1016/j.ijmecsci.2023.108540.

[23] X. Li, M. Ichchou, A. Zine, N. Bouhaddi, P. Fossat, Wavenumber identification of 1D complex structures using algebraic wavenumber identification

(awi) technique under complex conditions, Journal of Sound and Vibration 548 (2023). doi:10.1016/j.jsv.2022.117524.

[24] D. Beli, A. T. Fabro, M. Ruzzene, J. R. F. Arruda, Wave attenuation and trapping in 3D printed cantilever-in-mass metamaterials with spatially correlated variability, Scientific Reports 9 (5617) (2019) 1–11. doi:10.1038/s41598-019-41999-0.

[25] D. Beli, J. R. F. Arruda, M. Ruzzene, Wave propagation in elastic metamaterial beams and plates with interconnected resonators, International Journal of Solids and Structures 139-140 (2018) 105–120. doi:10.1016/j.ijsolstr.2018.01.027.

[26] J. Chen, J. Chen, H. Wang, L. He, B. Huang, S. Dadbakhsh, P. Bartolo, Fabrication and development of mechanical metamaterials via additive manufacturing for biomedical applications: a review, International Journal of Extreme Manufacturing 7 (2025) 012001. doi:10.1088/2631-7990/ad88e3.

[27] X. Wu, Y. Su, J. Shi, Perspective of additive manufacturing for metamaterials development (2019). doi:10.1088/1361-665X/ab2eb6.

[28] P. Suhas, J. D. Quadros, Y. I. Mogul, M. Mohin, A. Aabid, M. Baig, O. S. Ahmed, A review on mechanical metamaterials and additive manufacturing techniques for biomedical applications (2024). doi:10.1039/d4ma00874j.

[29] D. Sharma, S. S. Hiremath, Additively manufactured mechanical metamaterials based on triply periodic minimal surfaces: Performance, challenges, and application, Mechanics of Advanced Materials and Structures 29 (2022) 5077–5107. doi:10.1080/15376494.2021.1948151.

[30] Z. Zeng, S. Gao, D. K. Pokkalla, S. Zhang, C. Han, F. Liu, Z. Xiao, S. Y. Kandukuri, Y. Liu, K. Zhou, Additive manufacturing of metallic metamaterials with enhanced mechanical properties enabled by microstructural and

structural design, International Journal of Machine Tools and Manufacture 199 (2024). doi:10.1016/j.ijmachtools.2024.104172.

[31] D. B. Pham, S. C. Huang, Composite metastructure with tunable ultra-wide low-frequency three-dimensional band gaps for vibration and noise control, Scientific reports 14 (2024) 22890. doi:10.1038/s41598-024-73909-4.

[32] L. H. M. Ribeiro, C. Claeys, A. T. Fabro, D. Chronopoulos, J. R. F. Arruda, Robust optimization of a 3D printed periodic frame structure using the inferred characterization of the additive manufacturing system, Mechanical Systems and Signal Processing 217 (2024). doi:10.1016/j.ymssp.2024.111515.

[33] W. Anigbogu, H. Nguyen, H. Bardaweel, Layered metamaterial beam structures with local resonators for vibration attenuation: Model and experiment, Frontiers in Mechanical Engineering 7 (2021). doi:10.3389/fmech.2021.768508.

[34] Y. Li, X. Li, J. Ding, Broadband low-frequency flexural wave attenuation in beam-type metastructures with double-sides inertial amplified resonators, Journal of Vibration and Control 29 (21-22) (2023) 4924–4934. doi:10.1177/10775463221126930.

[35] L. Zhao, Z. Lu, H. Ding, L. Chen, A viscoelastic metamaterial beam for integrated vibration isolation and energy harvesting, Applied Mathematics and Mechanics (English Edition) 45 (2024) 1243–1260. doi:10.1007/s10483-024-3159-7.

[36] X. Fan, X. Mao, Y. Dong, H. Liu, M. Shao, L. Wang, Tunable bandgaps of a metamaterial beam with nonlinear magnetic resonators, Nonlinear Dynamics 112 (2024) 9743–9765. doi:10.1007/s11071-024-09627-3.

[37] J. Tang, T. Wang, Y. Li, H. Lin, H. Chen, D. Cao, Low-frequency band gap vibration isolation of local-resonant metamaterial beam with curved-

beam resonators, Mechanics of Advanced Materials and Structures (2024). doi:10.1080/15376494.2024.2434196.

[38] G. Wang, F. Shi, Z. Chen, Y. Yu, C. W. Lim, Controllable flexural wave bandgap in extensible metamaterial beams with embedded multiple resonators, Continuum Mechanics and Thermodynamics (9 2023). doi:10.1007/s00161-023-01228-6.

[39] G. Failla, A. Burlon, A. F. Russillo, A novel metamaterial multiple beam structure with internal local resonance, Acta Mechanica 235 (2024) 5885–5903. doi:10.1007/s00707-024-04006-w.

[40] Y. Xiao, J. Wen, D. Yu, X. Wen, Flexural wave propagation in beams with periodically attached vibration absorbers: Band-gap behavior and band formation mechanisms, Journal of Sound and Vibration 332 (4) (2013) 867–893. doi:10.1016/j.jsv.2012.09.035.

[41] E. J. P. Miranda Jr., J. M. S. Dos Santos, Flexural wave band gaps in multi-resonator elastic metamaterial Timoshenko beams, Wave Motion 91 (2019) 102391. doi:10.1016/j.wavemoti.2019.102391.

[42] J. Chen, B. Sharma, C. Sun, Dynamic behaviour of sandwich structure containing spring-mass resonators, Composite Structures 93 (8) (2011) 2120–2125. doi:10.1016/j.compstruct.2011.02.007.

[43] L. Ding, B. Ding, Q.-Y. Wu, H.-P. Zhu, Flexural wave propagation in a double-beam system interconnected by local resonators with two degrees of freedom, Journal of Engineering Mechanics 149 (2023). doi:10.1061/JENMDT.EMENG-6762.

[44] R. Lakes, Materials with structure hierarchy, Nature 361 (1993) 511–515. doi:10.1038/361511a05.

[45] V. F. Dal Poggetto, E. J. Miranda Jr., J. M. C. Dos Santos, N. M. Pugno, Wave attenuation in viscoelastic hierarchical plates, International Jour-

nal of Mechanical Sciences 236 (2022) 107763. doi:10.1016/j.ijmecsci.2022.107763.

[46] D. Mu, K. Wang, H. Shu, J. Lu, Metamaterial beams with graded two-stage inertial amplification and elastic foundation, International Journal of Mechanical Sciences 236 (2022) 107761. doi:10.1016/j.ijmecsci.2022.107761.

[47] Y. Jian, L. Tang, G. Hu, Z. Li, K. C. Aw, Design of graded piezoelectric metamaterial beam with spatial variation of electrodes, International Journal of Mechanical Sciences 218 (2022) 107068. doi:10.1016/j.ijmecsci.2022.107068.

[48] Y. Jian, G. Hu, L. Tang, W. Tang, M. Abdi, K. C. Aw, Analytical and experimental study of a metamaterial beam with grading piezoelectric transducers for vibration attenuation band widening, Engineering Structures 275 (2023) 115091. doi:10.1016/j.engstruct.2022.115091.

[49] Y. Sun, Q. Han, C. Li, Novel hybrid-controlled graded metamaterial beam for bandgap tuning and wave attenuation, European Journal of Mechanics - A/Solids 103 (2024) 105178. doi:10.1016/j.euromechsol.2023.105178.

[50] C. S. Schimidt, L. P. R. de Oliveira, C. De Marqui, Vibro-acoustic performance of graded piezoelectric metamaterial plates, Composite Structures 327 (2024) 117656. doi:10.1016/j.compstruct.2023.117656.

[51] J. Lou, H. Fan, A. Zhang, M. Xu, J. Du, A graded acoustic metamaterial rod enabling ultra-broadband vibration attenuation and rainbow reflection, Thin-Walled Structures 198 (2024) 111716. doi:10.1016/j.tws.2024.111716.

[52] X. Kuci, M. G. Geers, V. G. Kouznetsova, Towards design of a gradient locally resonant acoustic metasurface for negative reflection, Journal of the Mechanics and Physics of Solids 187 (2024). doi:10.1016/j.jmps.2024.105632.

[53] P. Liu, H. Xiang, A space-adiabatic theorem for longitudinal and transversal wave motion analysis of graded metamaterials, Journal of Intelligent Material Systems and Structures (2024). doi:10.1177/1045389x241276215.

[54] L. Iorio, J. M. D. Ponti, F. Maspero, R. Ardito, Roton-like dispersion via polarisation change for elastic wave energy control in graded delay-lines, Journal of Sound and Vibration 572 (2024). doi:10.1016/j.jsv.2023.118167.

[55] L. S. Pillarisetti, D. G. Guzman, J. Keirn, S. Sridhar, C. Lissenden, M. Frecker, P. Shokouhi, Frequency bandgap enhancement in locally resonant metasurfaces for S0 lamb wave mode using topology-optimized resonators, Journal of Applied Physics 137 (2025). doi:10.1063/5.0244722.

[56] L. Rosafalco, J. M. D. Ponti, L. Iorio, R. V. Craster, R. Ardito, A. Corigliano, Reinforcement learning optimisation for graded metamaterial design using a physical-based constraint on the state representation and action space, Scientific Reports 13 (2023). doi:10.1038/s41598-023-48927-3.

[57] A. Banerjee, Non-dimensional analysis of the elastic beam having periodic linear spring mass resonators, Meccanica 55 (2020) 1181–1191. doi:10.1007/s11012-020-01151-z.

[58] A. Banerjee, R. Das, E. P. Calius, Frequency graded 1D metamaterials: A study on the attenuation bands, Journal of Applied Physics 122 (7) (2017) 075101. doi:10.1063/1.4998446.

[59] A. Banerjee, Flexural waves in graded metabeam lattice, Physics Letters A 388 (2021) 127057. doi:10.1016/j.physleta.2020.127057.

[60] G. Hu, A. C. M. Austin, V. Sorokin, L. Tang, Metamaterial beam with graded local resonators for broadband vibration suppression, Mechanical

Systems and Signal Processing 146 (2021) 106982. doi:10.1016/j.ymssp.2020.106982.

[61] J. M. D. Ponti, L. Iorio, E. Riva, F. Braghin, A. Corigliano, R. Ardito, Enhanced energy harvesting of flexural waves in elastic beams by bending mode of graded resonators, Frontiers in Materials 8 (11 2021). doi:10.3389/fmats.2021.745141.

[62] B. Zhao, H. R. Thomsen, J. M. D. Ponti, E. Riva, B. V. Damme, A. Bergamini, E. Chatzi, A. Colombi, A graded metamaterial for broadband and high-capability piezoelectric energy harvesting, Energy Conversion and Management 269 (2022). doi:10.1016/j.enconman.2022.116056.

[63] J. M. D. Ponti, A. Colombi, R. Ardito, F. Braghin, A. Corigliano, R. V. Craster, Graded elastic metasurface for enhanced energy harvesting, New Journal of Physics 22 (2020). doi:10.1088/1367-2630/ab6062.

[64] L. Rosafalco, J. M. D. Ponti, L. Iorio, R. Ardito, A. Corigliano, Optimised graded metamaterials for mechanical energy confinement and amplification via reinforcement learning, European Journal of Mechanics, A/Solids 99 (2023). doi:10.1016/j.euromechsol.2023.104947.

[65] Z. Wang, X. Lu, Z. Guo, Z. Li, Z. Lei, K. Zeng, Y. Zhao, Gradient fabry-pérot acoustic metamaterials enable rainbow-trapping enhanced broadband sound insulation, International Journal of Mechanical Sciences (2025) 110056doi:10.1016/j.ijmecsci.2025.110056.

[66] J. M. D. Ponti, L. Iorio, R. Ardito, Graded elastic meta-waveguides for rainbow reflection, trapping and mode conversion, EPJ Applied Metamaterials 9 (2022). doi:10.1051/epjam/2022004.

[67] F. Maspero, J. M. D. Ponti, L. Iorio, A. Esposito, R. Bertacco, A. D. Matteo, A. Corigliano, R. Ardito, Phononic graded meta-MEMS for elastic

wave amplification and filtering, Journal of Microelectromechanical Systems 32 (2023) 522–528. doi:10.1109/JMEMS.2023.3320198.

[68] J. D. Ponti, L. Iorio, M. Rosso, F. Maspero, A. Esposito, T. A. Afifi, M. Riani, G. Gattere, A. D. Matteo, A. Corigliano, R. Ardito, Graded micro-resonators for enhanced sensing and energy harvesting in MEMS with lead-free piezoelectric materials, in: 2024 IEEE 23rd International Conference on Micro and Miniature Power Systems, Self-Powered Sensors and Energy Autonomous Devices (PowerMEMS), IEEE, 2024, pp. 155–158. doi:10.1109/PowerMEMS63147.2024.10814200.

[69] L. Iorio, J. M. D. Ponti, R. Ardito, A. Corigliano, Graded meta-waveguides for elastic energy splitting, in: Materials Research Proceedings, Vol. 26, Association of American Publishers, 2023, pp. 529–534. doi:10.21741/9781644902431-86.

[70] J. M. D. Ponti, L. Iorio, E. Riva, R. Ardito, F. Braghin, A. Corigliano, Selective mode conversion and rainbow trapping via graded elastic waveguides, Physical Review Applied 16 (2021). doi:10.1103/PhysRevApplied.16.034028.

[71] S. V. Kuznetsov, Cauchy six-dimensional formalism for lamb waves in multilayered plates, ISRN Mechanical Engineering 2013 (2013). doi:10.1155/2013/698706.

[72] S. V. Kuznetsov, Cauchy formalism in the theory of acoustic surface waves, Mechanics of Solids 55 (2020) 482–489. doi:10.3103/S0025654420040068.

[73] D. F. Parker, The stroh formalism for elastic surface waves of general profile, Proceedings of the Royal Society A: Mathematical, Physical and Engineering Sciences 469 (12 2013). doi:10.1098/rspa.2013.0301.

[74] E. J. Miranda, V. F. D. Poggetto, N. M. Pugno, J. M. D. Santos, Extended plane wave expansion formulation for viscoelastic phononic thin plates, Wave Motion 123 (2023). doi:10.1016/j.wavemoti.2023.103222.

[75] V. B. Oliveira, C. G. S. Filho, J. M. D. Santos, E. J. Miranda, Wave attenuation in 1-D viscoelastic periodic structures with thermal effects, Journal of the Brazilian Society of Mechanical Sciences and Engineering 46 (2024). doi:10.1007/s40430-023-04624-w.

[76] L. F. Schalcher, J. M. Santos, E. J. Miranda, Extended plane wave expansion formulation for 1-D viscoelastic phononic crystals, Partial Differential Equations in Applied Mathematics 7 (2023). doi:10.1016/j.padiff.2023.100489.

[77] M. C. Santos, C. G. Filho, E. J. Miranda, A. Sinatora, Formulation of the extended plane wave expansion for in-plane and out-of-plane vibrations in viscoelastic phononic thin plates under a constant temperature field, ZAMM Zeitschrift fur Angewandte Mathematik und Mechanik 105 (2025). doi:10.1002/zamm.202400532.

[78] E. Miranda, S. Rodrigues, C. Aranas, J. Dos Santos, Plane wave expansion and extended plane wave expansion formulations for mindlin-reissner elastic metamaterial thick plates, Journal of Mathematical Analysis and Applications 505 (2) (2022) 125503. doi:https://doi.org/10.1016/j.jmaa.2021.125503.

[79] E. J. P. Miranda Jr., J. M. C. Dos Santos, Flexural wave band gaps in phononic crystal Euler-Bernoulli beams using wave finite element and plane wave expansion methods, Materials Research 20 (Suppl.2) (2017) 729–742. doi:10.1590/1980-5373-MR-2016-0877.

[80] J.-M. Mencik, On the low- and mid-frequency forced response of elastic structures using wave finite elements with one-dimensional propagation, Computers and Structures 88 (2010) 674–689. doi:10.1016/j.compstruc.2010.02.006.

[81] B. Yuan, V. F. Humphrey, J. Wen, X. Wen, On the coupling of resonance and Bragg scattering effects in three-dimensional locally resonant sonic ma-

terials, Ultrasonics 53 (2013) 1332–1343. doi:10.1016/j.ultras.2013.03.019.

[82] M. Chen, D. Meng, H. Zhang, H. Jiang, Y. Wang, Resonance-coupling effect on broad band gap formation in locally resonant sonic metamaterials, Wave Motion 63 (2016) 111–119. doi:10.1016/j.wavemoti.2016.02.003.

[83] A. O. Krushynska, M. Miniaci, F. Bosia, N. M. Pugno, Coupling local resonance with Bragg band gaps in single-phase mechanical metamaterials, Extreme Mechanics Letters 12 (2017) 30–36. doi:10.1016/j.eml.2016.10.004.

[84] Z. Deng, B. Zhang, K. Zhang, L. Peng, P. Liu, Q. Sun, F. Pang, The coupled band gap of longitudinal wave in metamaterial-based double-rod containing resonators, Journal of Vibration and Control (2024). doi:10.1177/10775463241276706.

[85] Y. Sun, Q. Han, T. Jiang, C. Li, Coupled bandgap properties and wave attenuation in the piezoelectric metamaterial beam on periodic elastic foundation, Applied Mathematical Modelling 125 (2024) 293–310. doi:10.1016/j.apm.2023.09.030.

[86] D. J. Mead, A general theory of harmonic wave propagation in linear periodic systems with multiple coupling, Journal of Sound and Vibration 27 (2) (1973) 235–260. doi:10.1016/0022-460X(73)90064-3.

[87] W. Zhong, F. Williams, On the direct solution of wave propagation for repetitive structures, Journal of Sound and Vibration 181 (3) (1995) 485–501. doi:10.1006/jsvi.1995.0153.

[88] P. B. Silva, J.-M. Mencik, J. R. F. Arruda, On the use of the wave finite element method for passive vibration control of periodic structures, Advances in Aircraft and Spacecraft Science 3 (3) (2016) 299–315. doi:10.12989/aas.2016.3.3.299.